CAP-95-93R
BNL- 48958

WAKE-FIELD AND SPACE CHARGE EFFECTS ON HIGH BRIGHTNESS BEAMS CALCULATIONS AND MEASURED RESULTS FOR THE LASER DRIVEN PHOTOELECTRONS AT BNL-ATF

ZOHREH PARSA

CENTER FOR ACCELERATOR PHYSICS
BROOKHAVEN NATIONAL LABORATORY

ASSOCIATED UNIVERSITIES, INC.
UNDER CONTRACT NO. DE-AC02-76CH00016 WITH THE
UNITED STATES DEPARTMENT OF ENERGY

PRESENTED AT THE THE SYMPOSIUM ON ACCELERATOR PHYSICS AND MODELING , ON 9/17/91 @ Brookhaven National Laboratory
UPTON, NEW YORK 11973

WAKE-FIELD AND SPACE CHARGE EFFECTS ON HIGH BRIGHTNESS BEAMS - CALCULATIONS AND MEASURED RESULTS FOR THE LASER EXCITED PHOTOELECTRONS AT BNL-ATF

Zohreh Parsa
Brookhaven National Laboratory
Upton, New York 11973

Abstract.

We discuss the formalism used to study the effects of the interactions between the highly charged particles and the fields in the accelerating structure, including space charge and wake fields. Some of our calculations and numerical simulation results obtained for the Brookhaven National Laboratory (BNL) high-brightness photoelectron beam at the Accelerator Test Facility (ATF) and the measured data at ATF are also included.

* Work performed under the auspices of the U.S. Department of Energy.

TABLE OF CONTENTS

Section

- Introduction
- Formalism
- ATF Injection System
- Beam Analysis
- Measured Data
- Acknowledgement
- Summary
- References
- Figure Captions

I. Introduction

The effects of the interaction between the highly charged particles and the fields in an accelerating structure are discussed. In Section II, we present an overview of formalism used to study the behavior of the field and the dynamics of the highly charged bunch of particles in presence of an accelerating field, space charge forces (due to self field of the bunch), and the wake field (arising from the interaction of the cavity surface and the self field of the bunch). Since high-brightness, laser-driven radio-frequency (rf) guns, are potential sources of high-current, low-emittance and short-bunch beams of electrons for application to new methods of acceleration and FELs in section III we discuss the calculated results and numerical simulations for the example of the BNL photocathode gun at ATF. Where To achieve high brightness and rapid acceleration, an rf gun operating at 2.856 GHz, with 1-1/2 cells, π- mode resonant, disc-loaded structure (with cathode placed at the start of the first 1/2 cell), has been designed [Fig. 6] and operated as the injector for the two S-band linac sections at the BNL Accelerator Test Facility (ATF). In section IV, the measured data from the BNL Accelerator Test Facility is also included.

Preliminary data from ATF indicate after illuminating the cathode with a pulse of 0.1 mJ/cm^2 (reached in 10 ps) an "enhanced" emission mode is set, during which time (50 ns) a large amount of charge is generated and accelerated in the gun after which time the gun energy is depleted. The mechanism and the damage to the cathode is under investigation at ATF.

A summary and references are given in sections V and VI followed by the Figure captions in section VII.

II. Formalism

In this section, we present an overview of the formalism used to study the interaction of charged particle bunches with the fields inside the accelerating structures. In that consider the motion of highly charged bunches of electrons in an axisymmetrical Electromagnetic field. The wave equation can be presented as two uncoupled TE (E_ϕ, H_r, H_z), and TM (H_ϕ, E_r, E_z) sets of equations given below:

TE-like set:

$$\begin{cases} \dfrac{\partial^2 E_\phi}{\partial z^2} + \dfrac{1}{r}\dfrac{\partial}{\partial r}\left(r\dfrac{\partial E_\phi}{\partial r}\right) - \dfrac{E_\phi}{r^2} - \dfrac{1}{c^2}\dfrac{\partial^2 E_\phi}{\partial t^2} = \mu_o \dfrac{\partial J_\phi}{\partial t} \\ \dfrac{\partial^2 H_r}{\partial z^2} + \dfrac{\partial^2 H_r}{\partial r^2} - \dfrac{H_r}{r^2} - \dfrac{1}{c^2}\dfrac{\partial^2 H_r}{\partial t^2} = \dfrac{\partial J_\phi}{\partial z} \\ \dfrac{\partial^2 H_z}{\partial z^2} + \dfrac{\partial^2 H_z}{\partial r^2} - \dfrac{1}{c^2}\dfrac{\partial^2 H_z}{\partial t^2} = -\dfrac{1}{r}\dfrac{\partial (r J_\phi)}{\partial r} \end{cases} \qquad (1)$$

TM-like set:

$$\begin{cases} \dfrac{\partial^2 H_\phi}{\partial z^2} + \dfrac{1}{r}\dfrac{\partial}{\partial r}\left(r\dfrac{\partial H_\phi}{\partial r}\right) - \dfrac{H_\phi}{r^2} - \dfrac{1}{c^2}\dfrac{\partial^2 H_\phi}{\partial t^2} = \dfrac{\partial J_z}{\partial r} - \dfrac{\partial J_r}{\partial z} \\ \dfrac{\partial^2 E_r}{\partial z^2} + \dfrac{1}{r}\dfrac{\partial}{\partial r}\left(r\dfrac{\partial E_r}{\partial r}\right) - \dfrac{E_r}{r^2} - \dfrac{1}{c^2}\dfrac{\partial^2 E_r}{\partial t^2} = \dfrac{1}{\varepsilon_o}\dfrac{\partial \rho}{\partial r} + \mu_o \dfrac{\partial J_r}{\partial t} \\ \dfrac{\partial^2 E_z}{\partial z^2} + \dfrac{1}{r}\dfrac{\partial}{\partial r}\left(r\dfrac{\partial E_z}{\partial r}\right) - \dfrac{1}{c^2}\dfrac{\partial^2 E_z}{\partial t^2} = \dfrac{1}{\varepsilon_o}\dfrac{\partial \rho}{\partial z} + \mu_o \dfrac{\partial J_z}{\partial t} \end{cases} \qquad (2)$$

5) and functions (ϕ, J_r, J_z), over a mesh. In that one solves simultaneously the equations for the field propagation and the equation of motion for the particles. Where the effects of the EM interactions on the beam dynamics properties, such as emittance, energy spreads, etc., can be obtained [1] by knowing the field H_ϕ at each mesh point. For example, the equation can be integrated with respect to the standard Runge-Kutta method for a given charge distribution e.g. with

$$\rho_i\,(r, r_i, z, z_i) = e^{-\frac{(z-z_i)^2}{2\sigma_z^2} - \frac{(r-r_i)^2}{2\sigma_r^2}}\, e^{-\left(\frac{r\,r_i}{\sigma_r^2}\right)} \tag{6}$$

The corresponding current densities are:

$$J_z = \beta_{\|}^i \frac{c\;q_i}{(2\pi)^{3/2}\,\sigma_r^2\sigma_z^2}\, I_0\left(\frac{r\,r_i}{\sigma_r^2}\right) e^{-(z-z_i)^2/2\sigma_z^2} e^{\left(-r^2-r_i^2\right)/2\sigma_r^2} \tag{7}$$

$$J_r = \beta_{\perp}^i \frac{q_i c}{(2\pi)^{3/2}\,\sigma_r^2\sigma_z^2}\, I_1\left(\frac{r\,r_1}{\sigma_r^2}\right) e^{-(z-z_i)^2/2\sigma_z^2} e^{\left(-r^2-r_i^2\right)/2\sigma_r^2} \tag{8}$$

These guarantees gauge invariance ($\nabla \bullet \vec{E} - \rho/\epsilon = 0$) and satisfy the continuity equation.

In Eqs. (5–7), σ_r, σ_z are the charge and coordinates of the i-th particle, $\beta_{\perp i}$ and $\beta_{\|i}$ are the radial and axial components of the i-th particle beta, respectively, and I_0 and I_1 are the zeroth and first-order modified Bessel functions of the first kind. (additional formulation is given in [1]).

For clarity, we state the emittance definitions used in our analysis given in the next section. Normalized transverse emittance $(\epsilon_T^N) = \sqrt{x^2 p_x^2 - (x\;p_x)^2}$, and rms transverse emittance $= \sqrt{x^2 x'^2 - (x\;x'^2)}$. (For a discussion of emittance including higher order-moments, see [3]). The normalized beam brightness is defined as $B_N = I_P/8\pi(\epsilon_N^T)^2$ where I_P is the peak current.

Beam Analysis

In this section we present some of our calculations and simulation results obtained for initial designed specifications as well as for those indicated by the preliminary measurements at the BNL Accelerator Test Facility (ATF) [1]. With the standard design parameters: laser spot size σ_r = 3 mm, laser pulse width σ_z = 2ps (0.6 mm), charge of 1.0 nC, E_0 = 100 MV/m on the cathode in Figures I - VI (with initial phases $\phi_0 = 55°$, $\phi_0 = 63°$, $\phi_0 = 75°$, $\phi_0 = 45°$ respectively), we show the beam energy, transverse emittance ($\epsilon_T^N \pi$ mm mrad), the bunch rms length [in mm], rms radius, longitudinal emittance (ϵ_L^N), peak current [in A] etc. at the gun exit. These Figures illustrate the propagation of the bunch self field produced by the bunch as well as the image charge (i.e. the interaction between the bunch charge and current with the cathode surface). Wake field effects (i.e the interaction with the cavity surface) at various points along the cavity are also illustrated, e.g. see the radial electric field plots. These Figures also illustrate the dependance of the beam parameters on the initial phase angle, which can be used as a method for controlling the beam parameters at the gun exit (see Figure 5), e.g. emittance growth.

In Figures VII, with laser spot size σ_r = 1.25 mm, laser pulse width σ_z = 2ps (0.6 mm), charge of 0.9 nC, E_0 = 100 MV/m, and initial phase (ϕ_0) = 50°, we obtain the maximum energy (4.21 MeV) and minimum transverse emittance ($\epsilon_T^N = 9.8\ \pi$ mm mrad) at the gun exit ($z \simeq 98$ mm). The bunch rms length is 1.077 mm, rms radius is 3.17 mm, longitudinal emittance (ϵ_L^N) is 4.55 mm mrad and peak current is 188 A. After magnetic compression, the bunch rms length reduces to 0.967 mm and peak current increases to 212 A. The ranges of the exit parameters for the gun, with respect to changes in the initial phase ϕ_0, are given in Fig. VII-(1–2). The behavior of the beam (including rf, space charge and wake-field effects) are shown in Figs. VI-(3–7), at various points along the cavity. In Fig. VII-(3–4), the electric components of the bunch self-field are shown, where the change in the axial position of the peak in the radial electric field (dashed lines) with the increase in radius is due to the wake-field effect.

In Figures VIII-X variations in the standard parameters (noted above) are used as indicated by the recent measurements at ATF [1], including smaller values of σ_r and larger

In Figure XI, we present the results obtained with program PARMELA [4] for initial average axial electric field of 66.6 MV/m, laser pulse length of σ_z = 2.06 degrees (2Ps), σ_r = 3mm radius (design values) with the inclusion of space charge and image charges on the cathode. And in Figure XII, for the recent measured data with laser pulse length σ_z = 5Ps and σ_r = 1.25mm. A Gaussian shape is assumed for the distribution in both the radial and time dependance of the laser beam.

Earlier PARMELA results (as well as our other calculations) showed that the beam was too large through the beam line which resulted in a large emittance growth and a large beam loss. This analysis shows that a change in the 90° bends can improve the transport system which results in reduced emittance growth and eliminates the beam loss. The Pole pieces and perhaps the coils would be changed to provide some vertical focussing of the beam at the entrance and exit of the magnet. (Alternatively the pole pieces could be tapered to give a bending magnet with a nonuniform field to provide the required vertical focussing.)

The existing magnets have a 0° edge angle which means the beam enters and exits the magnets perpendicular to the magnet. The fringe field of the magnets cause the beam to bend slightly before the beam actually enters the magnet causing a vertical defocussing of the beam at the entrance and exit of each magnet. Also the two quad singlets which focus in the horizontal direction defocus in the vertical direction. In the present transport system the only vertical focussing elements are the two quad triplets before and after the bending system. Thus the beam gets too large in the vertical direction in this bending system even without space charge. Space charge only makes this condition worse. The modifications to the bending magnets is the addition of an 11° pole face rotation on the entrance and exits of the 90° bending magnets [4].

In Figs. XI and XII, Parameters were calculated from the cathode (labeled as element ne = 1) through the transport beam line to (element ne = 27) the linac entrance. For clarity, $ne = 1, 2, 3, 27$ corresponds to "cathode", "1st(1/2) cell", and "2nd(1/2) cell" and linac entrance respectively. Where number of particles are labeled as (np). The units are given for length (z) in [cm], emittance in [π cm − mrad], and energy w in [MeV].

In Section III, we showed numerical simulation of the exit beam parameters for (a few) different pulse lengths, as well as different charges, which illustrates the dependance of the emittance on the charge and laser pulse length.

The BNL rf-gun started operation in 1990. The peak momentum of 4.6 MeV/c, was obtained with 6.2 MW of rf power in the gun. Other parameters such as charge of up to 2.0 nC, peak current of 133 A, and emittance of 4 π mm mrad were also measured [1], (these measured data came from different runs).

The electron beam (transverse) emittance is measured with profile monitors PM1 and PM2 (for momentum dispersed beam) or PM3 and PM4 (for momentum recombine beam). shown in Figure 4. The emittance growth due to the injection system can be seen from the measurements obtained with PM3 and PM4 monitors. The emittance shown in Figure XIII are obtained by quadrupole variation method. That is by varying the strength of the quadrupole that proceeds the profile monitor and by observing the variations in the corresponding spot size on the same monitor. We need more data (after some of the laser etc. problems are resolved), for a comparison with theory and simulation results.*

---

* We acknowledge and thank members of ATF including K. Batchelor, J. Fisher, P. Russel and J. Xie for discussions and providing plots and information on the ATF preliminary data. Special thanks to Dr. J. Xie for providing information and copies of many papers including those listed in Ref. 10-14 which we used in our analysis of the ATF data.

entrance and exit of the magnet. Alternatively the pole pieces could be tapered to give a bending magnet with a nonuniform field to provide the required vertical focussing.

The existing magnets have a 0° edge angle which means the beam enters and exits the magnets perpendicular to the magnet. The fringe field of the magnets cause the beam to bend slightly before the beam actually enters the magnet causing a vertical defocussing of the beam at the entrance and exit of each magnet. The modifications to the bending magnets is the addition of an 11° pole face rotation on the entrance and exits of the 90° bending magnets [4].

An alternative is to eliminate the transport line completely and place the gun directly into the linac. In that we have studied various schemes. One that seems to be of interest is to leave the present system as shown in Fig. 4, and add a second entry port (a straight ahead injection line directly into the linac). E.g. place the gun (or a second gun, so the present gun can be used as is) at the location of the 2nd dipole (shown in Fig. 4), with a solenoid against the gun exit, followed by a quadrupole triplets into the linac [for more info. e.g. see our subsequent notes on alternate injection system for ATF].

We also presented some preliminary measurements for the BNL laser-driven rf gun (see Fig. XIII). Which indicate a larger value of laser pulse length ($\sigma_z > 5$ps) than 2 ps design value.

It was also observed [1] that after illuminating the cathode with a pulse of 0.1 mJ/cm^2 (reached in about 10 ps), an ("enhanced") emission mode set in during which (after 5 ns of build up time) a large amount of charge was generated and accelerated in the gun for 50 ns, after which the gun energy was reduced (lost).

Some of preliminary ATF data [1] indicated that the emittance ($\sim$ 4 mm-mrad) remained constant, when the charge was varied from 0.2 to 2 nC. This may have been due to the misalignment in the first quadrupole triplets [see Fig. 4], that is being corrected, and due to errors in the calibrations and /or interpretation of the preliminary measurements.

Our results for the beam energy at the gun exit compares well with the preliminary ATF data, (e.g. with Q, σ_z, E_0 given in column 2 of Table I), but predicts a larger range of values (not a constant value) for the emittance (when the charge was varied from .2 to

[3] Z. Parsa, "*On Beam Emittance and Invariants - Applications to ATF Beamline*". Proceedings. of the 2nd European Particle Accelerator Conf., Nice - France, June 12–16, 1990, Nile Ed., Frontiers, (1990); BNL Report BNL-44364 (1990) and Ref. therein.

[4] Z. Parsa, and L. Young, "*The BNL Photocathode Gun with the Code PARMELA*", Proceedings. of the 13th Int. FEL Conf., Santa Fe, NM., 26–30 Aug., 1991 ; Nucl. Inst. Meths. A318; BNL-46804 (1991);

Z. Parsa, and L. Young, "*On Design and Analysis of High Brightness Electron Source*", Proceedings. of the 2nd European Particle Accelerator Conf., Nice - France, June 12–16, 1990, Nile Ed., Frontiers, (1990); BNL Report BNL-44365 (1990) and Ref. therein:

L. Young, (Private comms.), PARMELA (1991).

[5] A. Pretti, (Private comm); L. Serafini (private comm.), C. Pagani et al, *itaca* (1990); ibid, Proc. EPAC, Rome, Ed. World Scientific, p. 866 (1988); Some simulations were made with a modified 1990 version of the program.

[6] Z. Parsa, "*Interactions Between Charged Particles and RF Space Charge and Wake Fields in an Accelerating Structure*", The Vancouver Meeting of Particles and Fields 91, Vol. 2, 1073, Ed. David Axen, Douglas Bayman and Martin Comyn; ibid, BNL Report BNL-48320 (1991).

[7] Z. Parsa, "*Effects of Variation of the Laser Pulse Width on the Laser Induced Photoelectrons*", Proceedings. of the 13th Int. FEL Conf., Santa Fe, NM., 26–30 Aug., 1991; Nucl. Inst. & Meth. A318; ibid, BNL-Report, BNL-46804 (1991).

[8] R. B. Palmer," *The Interdependence of Parameters for TeV Linear Colliders*", SLAC-PUB-4295, A (4/1987).

[9] Z. Parsa, "*Analysis of a High-Brightness Photoelectron Beam with Self-Field and Wake-Field Effects*" Proceedings of the 13th Int. FEL Conf., Santa Fe, NM., 26–30 Aug., 1991; Nucl. Inst. & Meth. A318; ibid, BNL-Report, BNL-46804 (1991).

[10] N. K. Sherman, Optical Eng. 28, No.10, 1114 (1989); References therein.

[11] M. Boussoukaya, H. Bergeret, R. Chehab, B. Leblond, and J. LeDuff, Nucl.Inst.& Meth. Phys. Res. A279, 405 (1989).

VII. FIGURE CAPTIONS

Figure 1 Block diagram of the Brookhaven Accelerator Test Facility.

Figure 2 The ATF experimental hall, showing how the beam is deflected into one of the three experimental beamlines.

Figure 3 Shows the ATF High-energy beamline.

Figure 4a Sketch of the BNL ATF injection system. The transport beamline from the gun to the linac entrance showing the positions of the magnetic elements. The preliminary emittance measurements were made at the profile monitors labeled as PM1, PM2.

Figure 4b Sketch of the BNL ATF injection system. The transport beamline from the gun to the linac entrance is shown and labeled. This is the same set up as in Fig. 4a where the elements are labeled.

Figure 5 Schematic plot of the BNL photocathode gun.

Figure 6 Block diagram of the ATF laser system.

Figure I–1 Shows plot of the $r * H_\phi$ =const. lines for 1 nC case, total field. For the design parameters with 100MV/m, $\phi_0 = 55$, σ_z= 2 ps, and σ_r= $3mm$.

Figure I–2 Shows plot of charge density distributions as functions of z and R (given by equations in section II).

Figure I–3 Shows plot of Current density distributions as functions of z at different radii, (see equations in section III).

Figure I–4 Shows plot of E_z (solid line) and E_r (dashed lines) vs z. This Figure shows the electric component of the bunch self field.

Figure I–5 Shows plot of E_z (solid line) and E_r (dashed lines) vs R.

Figure I–6 Shows plot of H_ϕ vs z. This Figure shows the effect of wake and bunch self - fields.

Figure I–7 Shows plot of H_ϕ vs R.

Figure I–8 Shows plot of Transverse Emittance vs z. Dashed line shows the normalized emittance; Solid line shows the rms emittance; and the third curve (with longer dashes) gives the normalized emittance associated with central slice of the bunch.

Figure II–10 Shows plot of Current density distributions as functions of z at different radii, (see equations in section III).

Figure II–11 Shows plot of propagation of the bunch self field produced by the bunch at average z position $\sim 48mm$.

Figure II–12 Shows plot of Transverse Emittance vs z. Dashed line shows the normalized emittance; Solid line shows the rms emittance; and the third curve (with longer dashes) gives the normalized emittance associated with central slice of the bunch.

Figure III–1 Shows plot of the $r * H_\phi$ = const lines for 1 nC case, total field, at output Z (Average) position of $\sim 98mm$.

Figure III–2 Shows plot of X vs X'; the transverse phase space.

Figure III–3 Shows plot of Transverse Emittance vs z. Dashed line shows the normalized emittances; Solid line shows the rms emittance; and the third curve (with longer dashes) gives the normalized emittance associated to with central slice of the bunch; at output phase of 425 degrees and initial phase of 65 degrees.

Figure III–4 Shows plot of Longitudinal Emittance vs z.

Figure III–5 Shows plot of Average Kinetic Energy (solid line) vs z.

Figure III–6 Shows plot of length of the bunch as function of z.

Figure IV–1 Shows plot of the $r * H_\phi$ = const lines for 1 nC case, total field.

Figure IV–2 Shows plot of X vs X'; the transverse phase space.

Figure IV–3 Shows plot of length of the bunch as function of z.

Figure V–1 Shows plot of the $r * H_\phi$ = const lines for 1 nC case, total field.

Figure V–2 Shows plot of Current density distributions as functions of z at different radii, (see equations in section III).

Figure V–3 Shows plot of Transverse Emittance vs z. Dashed line shows the normalized emittance; Solid line shows the rms emittance; and the third curve (with longer dashes) gives the normalized emittance associated with central slice of the bunch with initial phase of 45 degrees.

Figure VII–10 Shows plot of H_ϕ vs R. (2 ps case).

Figure VII–11 Shows plot of the $r * H_\phi$ = const lines.

Figure VII–12 Shows plot of X vs X'; the transverse phase space at Average Z = 98 mm for .9nC, (2 ps case).

Figure VII–13 Shows plot of $\rho div E$ vs R. (2 ps case).

Figure VII–14 Shows plot P_z/mc vs z. at Z average position of 98.24 mm. The solid line is the rms ellipse. (2 ps case).

Figure VII–15 Shows plot of E_z (solid line) and E_r (dashed lines) vs z. This Figure shows the electric component of the bunch self field. (2 ps case).

Figure VII–16 Shows plot of the $r * H_\phi$ = const lines for 1 nC case, total field, at output phase of 153 degrees. This plot shows the magnetic component of the bunch self-field. (2 ps case).

Figure VIII–1 Shows plot of the $r * H_\phi$ = const lines for 0.9 nC and 10ps case. Total field. (10 ps case).

Figure VIII–2 Shows plot of X vs X'; the transverse phase space at Average Z = 87 mm for .9nC and 10 ps case. (10 ps case).

Figure VIII–3 Longitudinal emittance [m rad] as a function of the bunch position z [mm]. The solid line (left scale) shows the normalized rms emittance, and the dashed lines shows $\delta\phi$ (right scale) along the cavity, with $\phi_0 = 40°$, and E_0 = 62 Mv/m on the cathode (as in the preliminary measured data). The boundary of the BNL rf-gun geometry is also shown. (10 ps case).

Figure VIII–4 Shows plot of length of the bunch as function of z. (10 ps).

Figure VIII–5 Shows plot of Average Kinetic Energy (solid line) vs z. (10 ps case).

Figure VIII–6 Shows plot of Transverse Emittance vs z. Dashed line shows the normalized emittances; Solid line shows the rms emittance; and the long-dashed line (right scale) shows the normalized emittance associated with a slice of the bunch (carrying $\sim$ 10 % of the total bunch charge), centered around z. The boundary of the BNL rf-gun geometry is also given. (10 ps case).

Figure IX–10 Shows plot of Current density distributions as functions of z at different radii, (see eqs in sect. III). (5 ps case).

Figure X–1 Shows plot of the $r * H_\phi$ = const lines for 0.9 nC and 2ps case. Total field.

Figure X–2 Shows plot of X vs X'; the transverse phase space at Average Z = 98.9 mm for .9nC and 2 ps case.

Figure X–3 Shows plot of the H_ϕ vs R. This plot shows the magnetic component of the field. (2 ps case).

Figure X–4 Shows plot P_r/mc vs R, (at Average Z = 94 mm). The solid line is the rms ellipse. (2 ps case).

Figure X–5 Shows plot of length of the bunch as function of z. (2 ps case).

Figure X–6 Transverse beam emittance [m rad] as a function of the bunch position z [mm], (from cathode to the gun exit), with σ_z = 2 ps. The dashed line shows the normalized rms emittance (right scale), the solid line shows the transverse emittance (left scale), and the long-dashed line (right scale) shows the normalized emittance associated with a slice of the bunch (carrying $\sim$ 10 % of the total bunch charge), centered around z. The boundary of the BNL rf-gun geometry is also given. (2 ps case).

Figure X–7 Shows plot of the H_ϕ vs z. This plot shows the magnetic component of the self-field. (2 ps case).

Figure X–8 Shows plot of E_z and E_r components of the field vs z at R=8.99 mm. (2 ps case).

Figure X–9 Shows plot of Average Kinetic Energy (solid line) vs z. (2 ps case).

Figure X–10 Longitudinal emittance [m rad] as a function of the bunch position z [mm]. The solid line (left scale) shows the normalized rms emittance, and the dashed lines shows $\delta\phi$ (right scale) along the cavity, with ϕ_0 = 40° , and E_0 = 62 Mv/m (and 2 ps) on the cathode (as in the preliminary measured data). The boundary of the BNL rf-gun geometry is also shown.

Figure X–11 Shows plot of E_z (solid line) and E_r (dashed lines) vs R. (2 ps case).

Figure XII–4 Shows phase space plots of the beam at the entrance to the linac (element 27). With the laser pulse length of σ_z = 5 ps and σ_r = 1.25 mm. The system will transfer 99.5 percent (with 11 degrees, pole face rotation) and the tuning of the quads are not as critical.

Figure XIII–1 Shows the vertical projections of the electron beam on a profile monitor as a function of quadrupole current where the measured emittance = 0.80+-0.09 mm-mrad.

Figure XIII–2 Shows the vertical projections of the electron beam on a profile monitor as a function of quadrupole current where the measured emittance = 0.77−-0.08 mm-mrad (this figure shows a different emittance scan than those given in Fig. XIII-1).

Figure XIII–3 Shows the vertical Emittance of the electron beam with variation in the spot size.

Figure XIII–4 Shows the vertical projections of the electron beam on a profile monitor as a function of quadrupole current where the measured emittance = 0.39+-0.25 mm-mrad. (this figure shows a different emittance scan than those given in Figs. XIII-1 and 2).

Figure XIII–5 Shows the vertical projections of the electron beam as a function of quadrupole current (this figure shows a different emittance scan than those given in Figs. XIII-1, 2 and 4).

Figure XIII–6 Shows the photoelectron–beam momentum as a function of the rf phase. The data points are the momentum measured in the beamline at ATF.

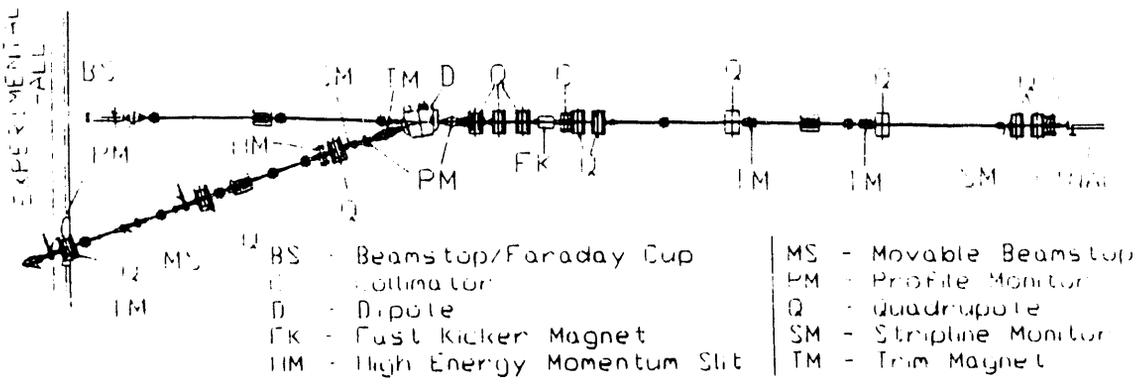

Figure 3 The ATF high-energy beamline. The beam exits the linac with an energy of 50 MeV and is transported into the experiment

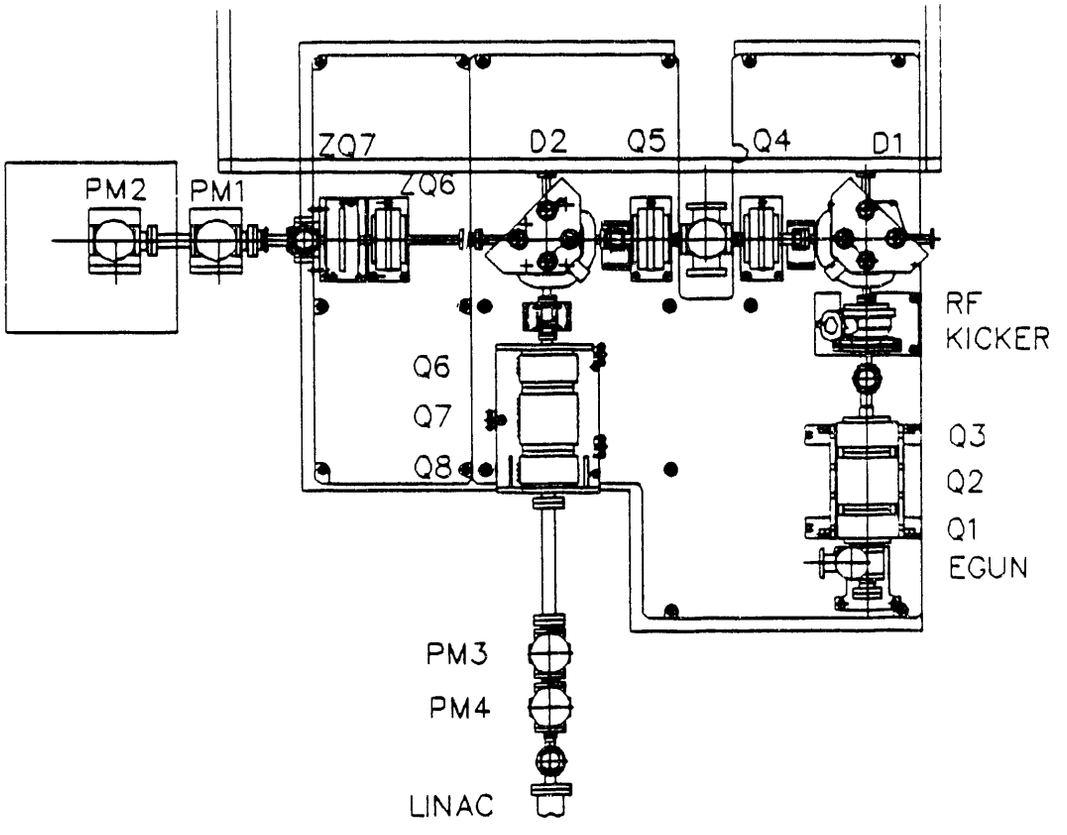

Figure 4a Transport beamline from the gun to the linac (ATF injection system).

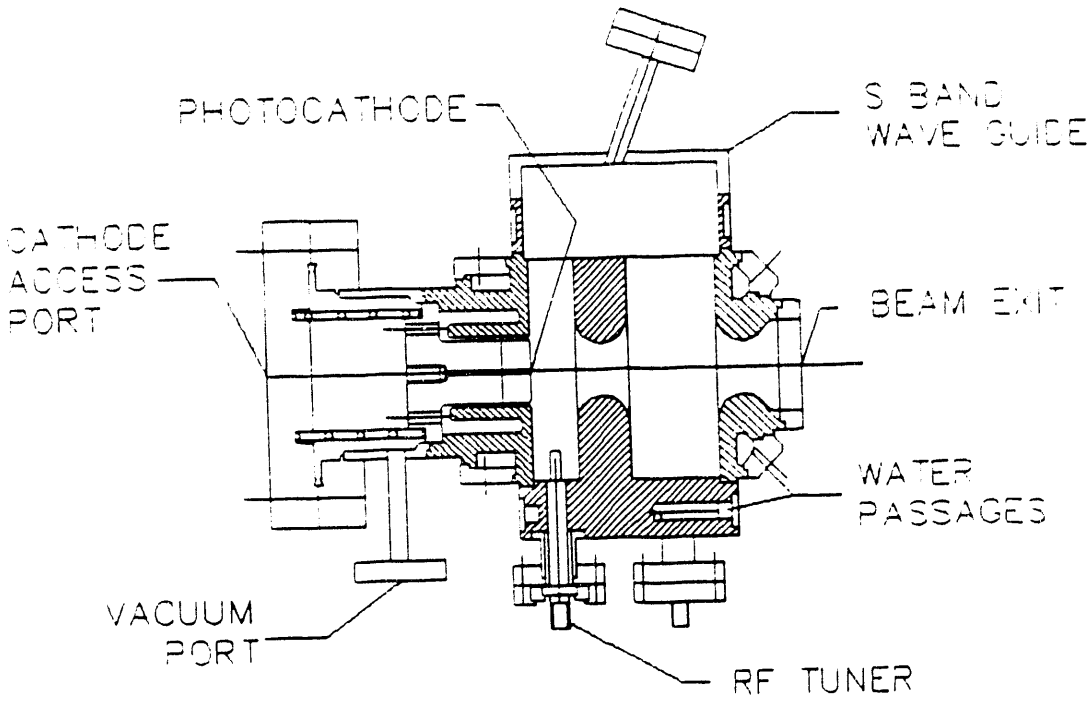

Figure 5 . Schematic Plot of the BNL Photocathode Gun.

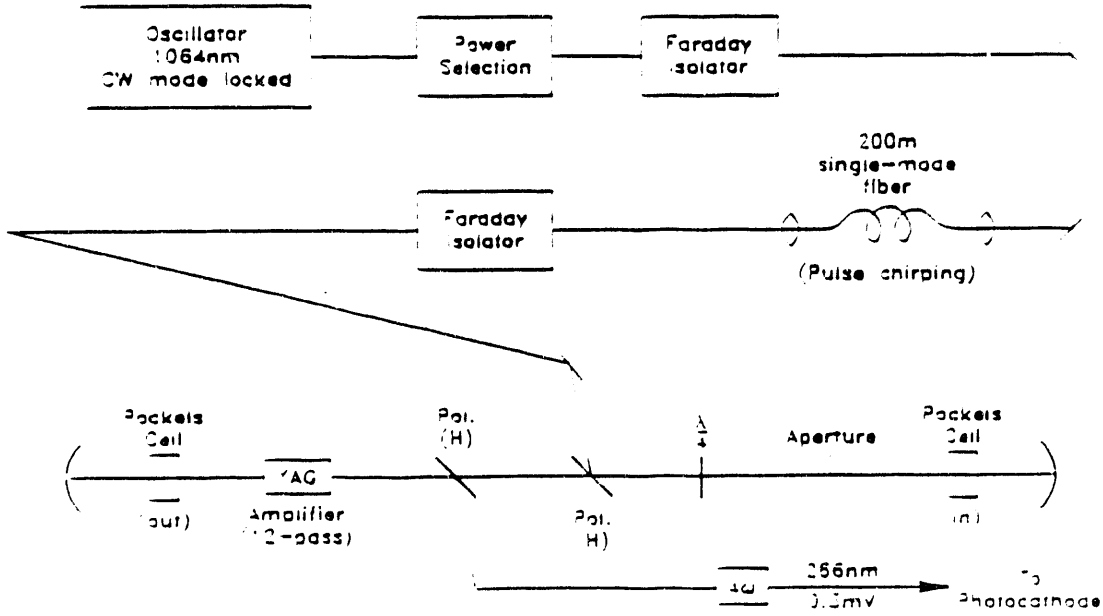

Figure 6 *Block diagram of the ATF laser system.*

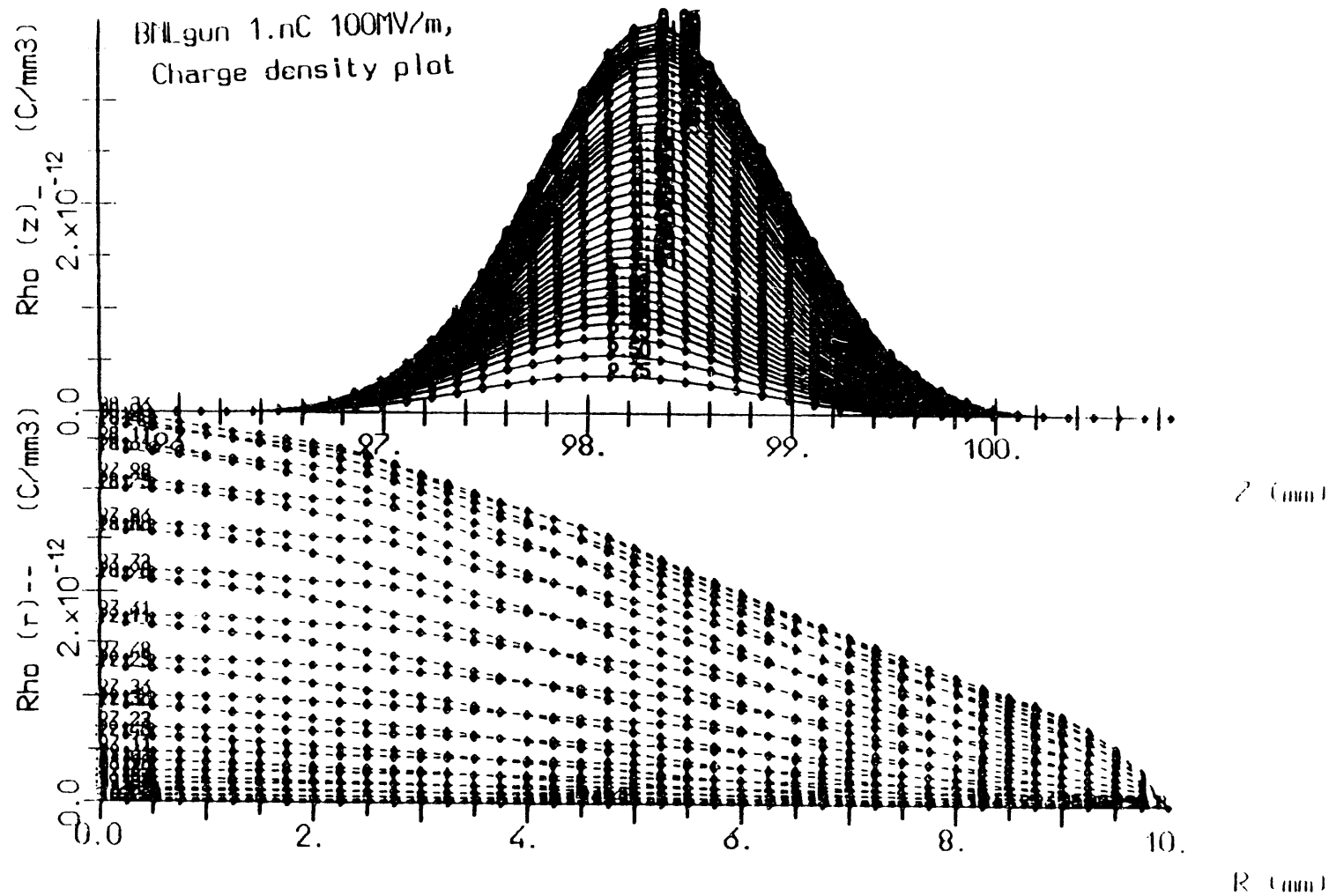

Figure I–2 Shows plot of charge density distributions as functions of z and R (given by equations in section II).

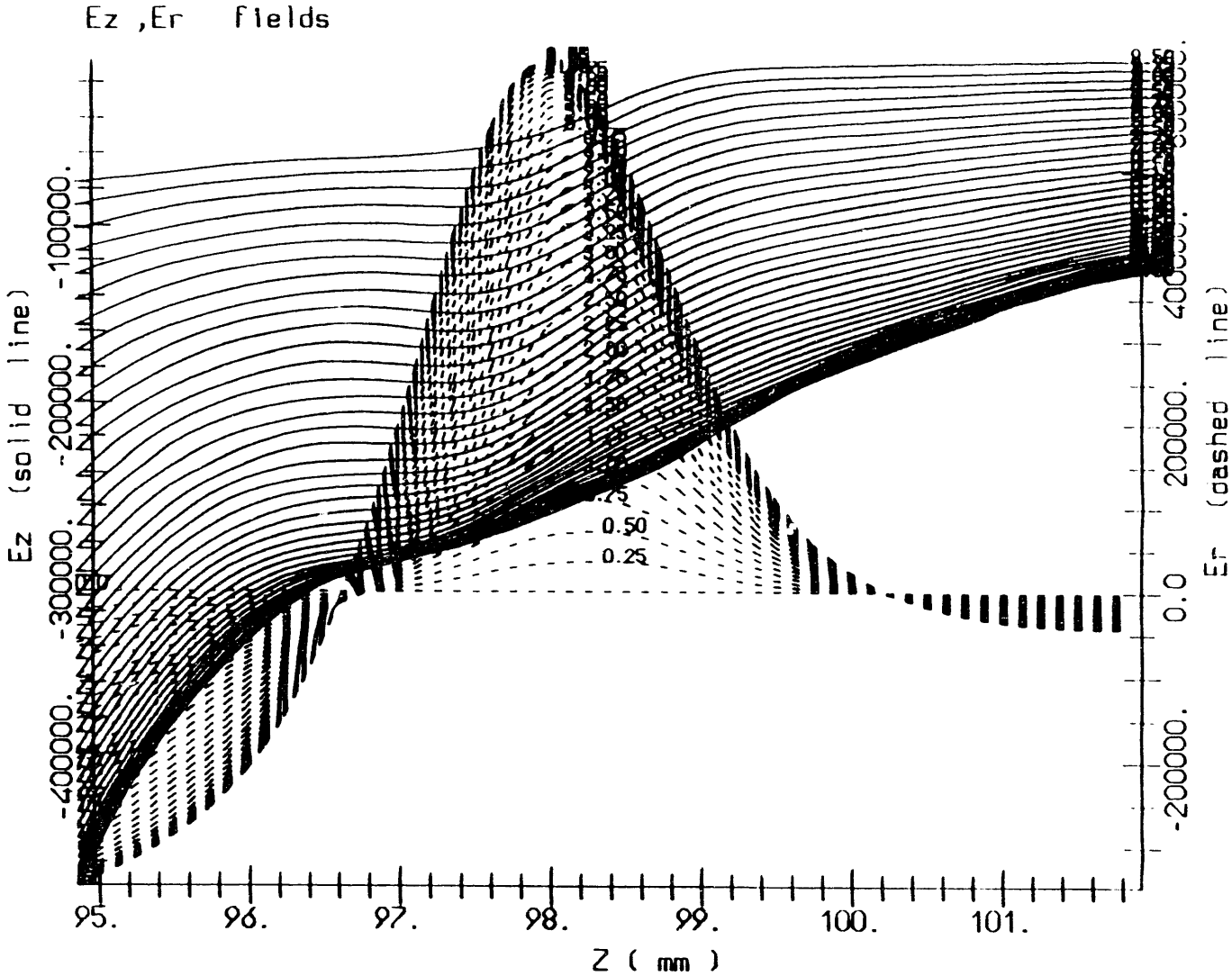

Figure I-4 shows plot of Ez (solid line) and Er (dashed lines) vs z, (the electric component of the bunch self field)

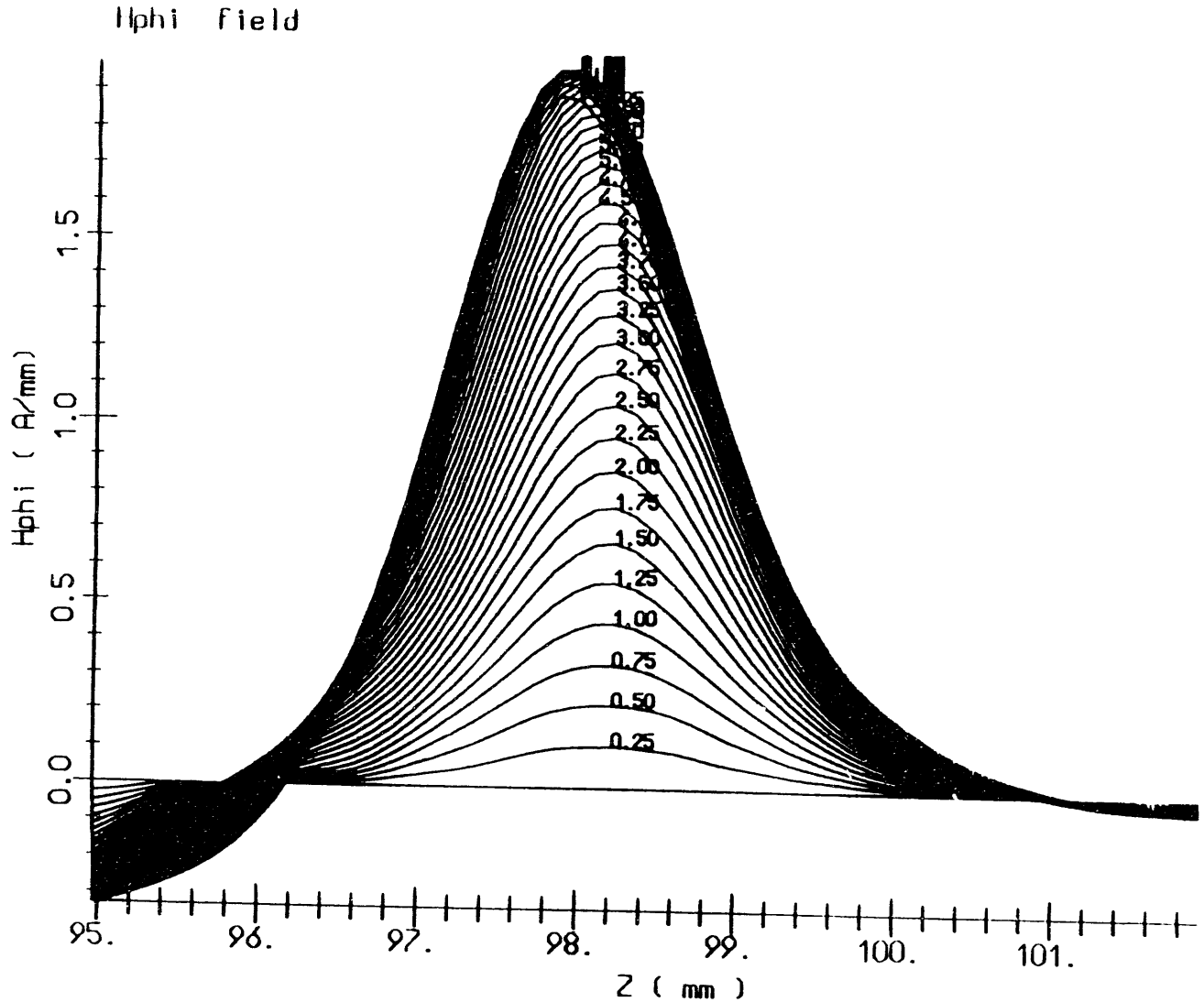

Figure I-6 shows plot of H_ϕ vs z, the effect of wake and the bunch self field.

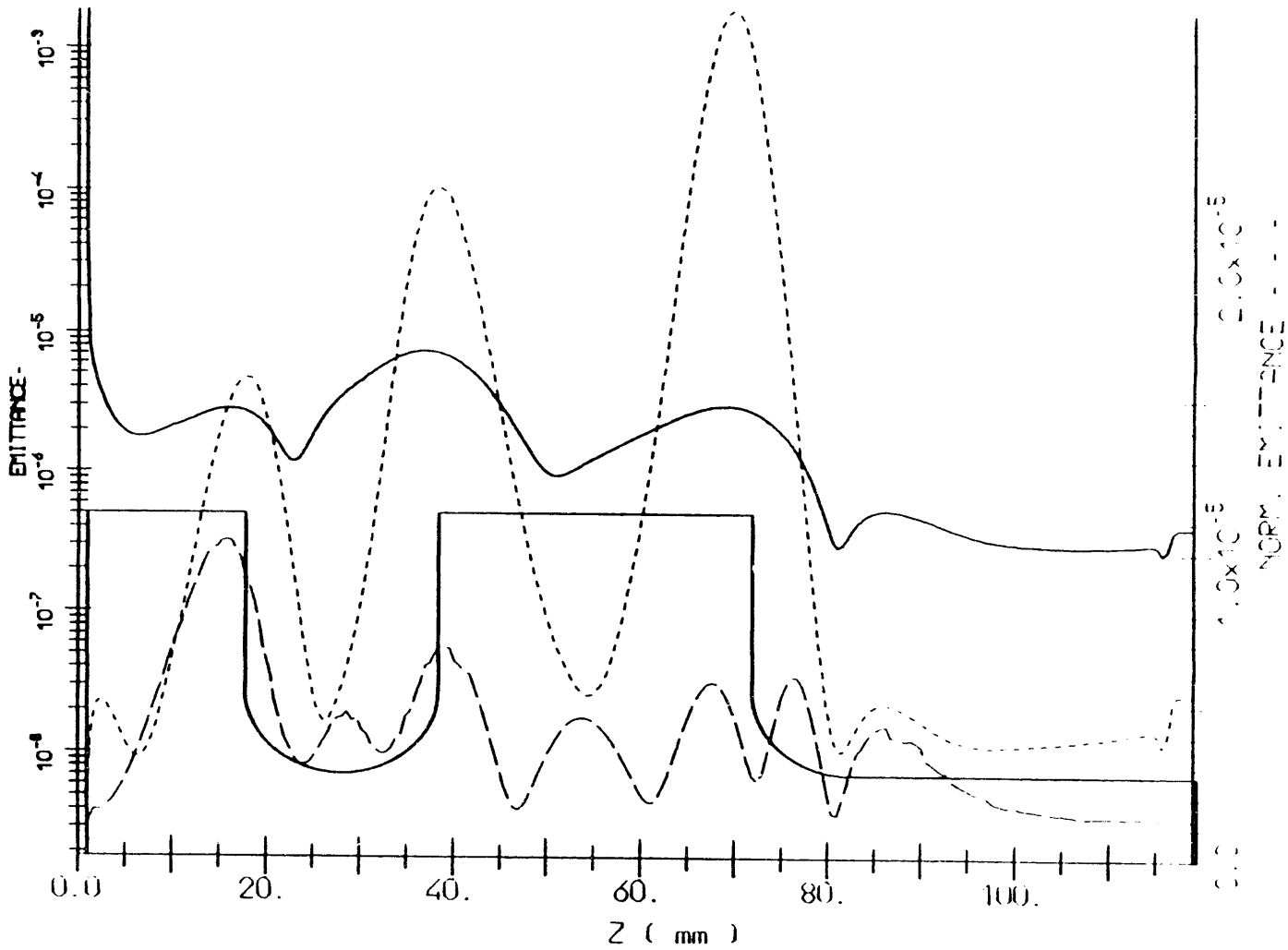

Figure I-8 shows plot of Transverse Emittance vs z. Dashed line shows the normalized emittances $\varepsilon_n = \sqrt{\langle x^2\rangle\langle p_x^2\rangle - \langle x p_x\rangle^2}$; Solid curve line shows the emittance $\varepsilon = \sqrt{\langle x^2\rangle\langle x'^2\rangle - \langle x x'\rangle^2}$ and third curve $\left(\varepsilon_n^{central}\right)$, gives ε_n associated to the central slice of the bunch.

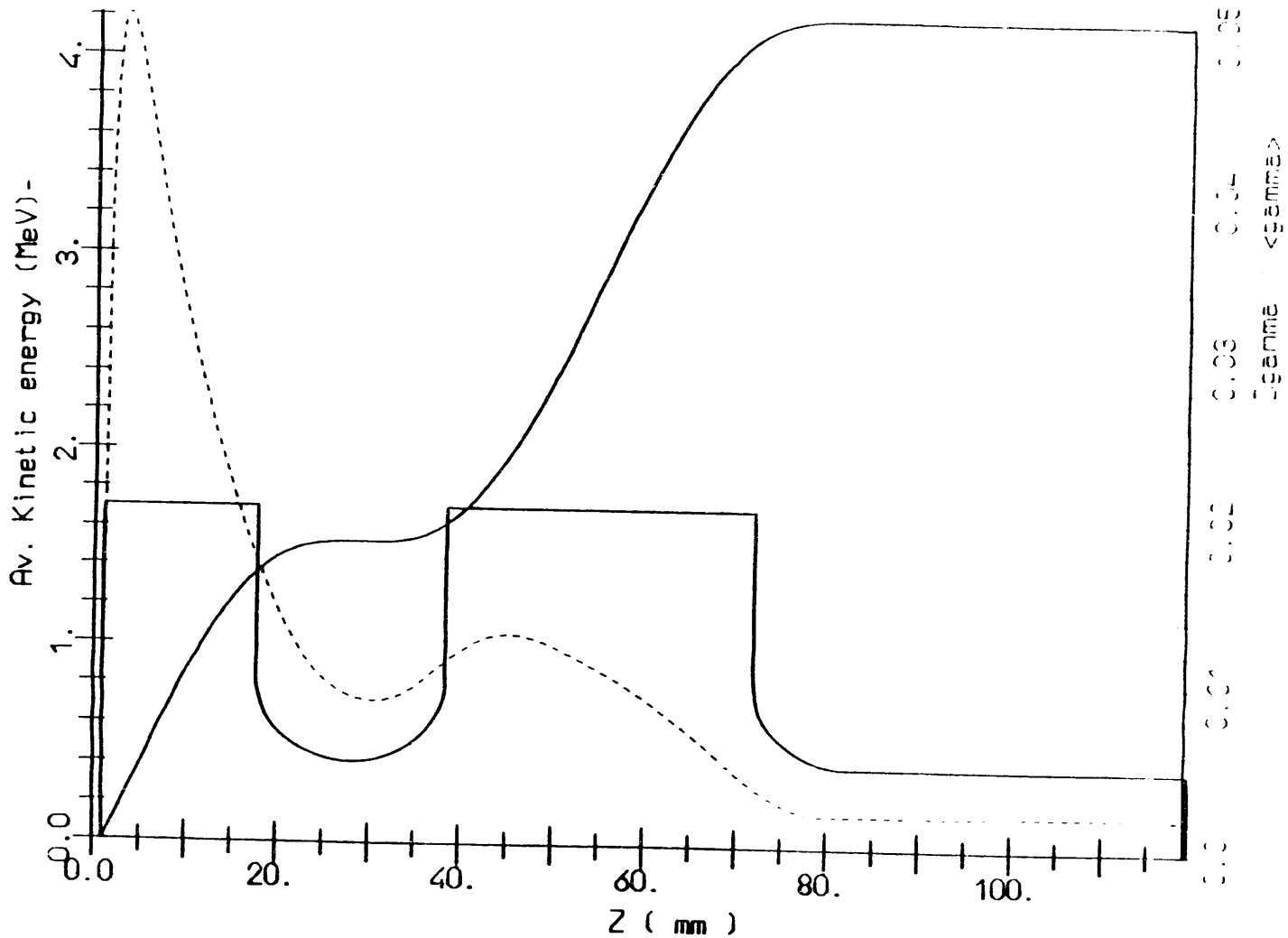

Figure I-10 shows plot of Average Kinetic Energy (solid line) and $\Delta\gamma/\langle\gamma\rangle$ (dashed line), vs z.

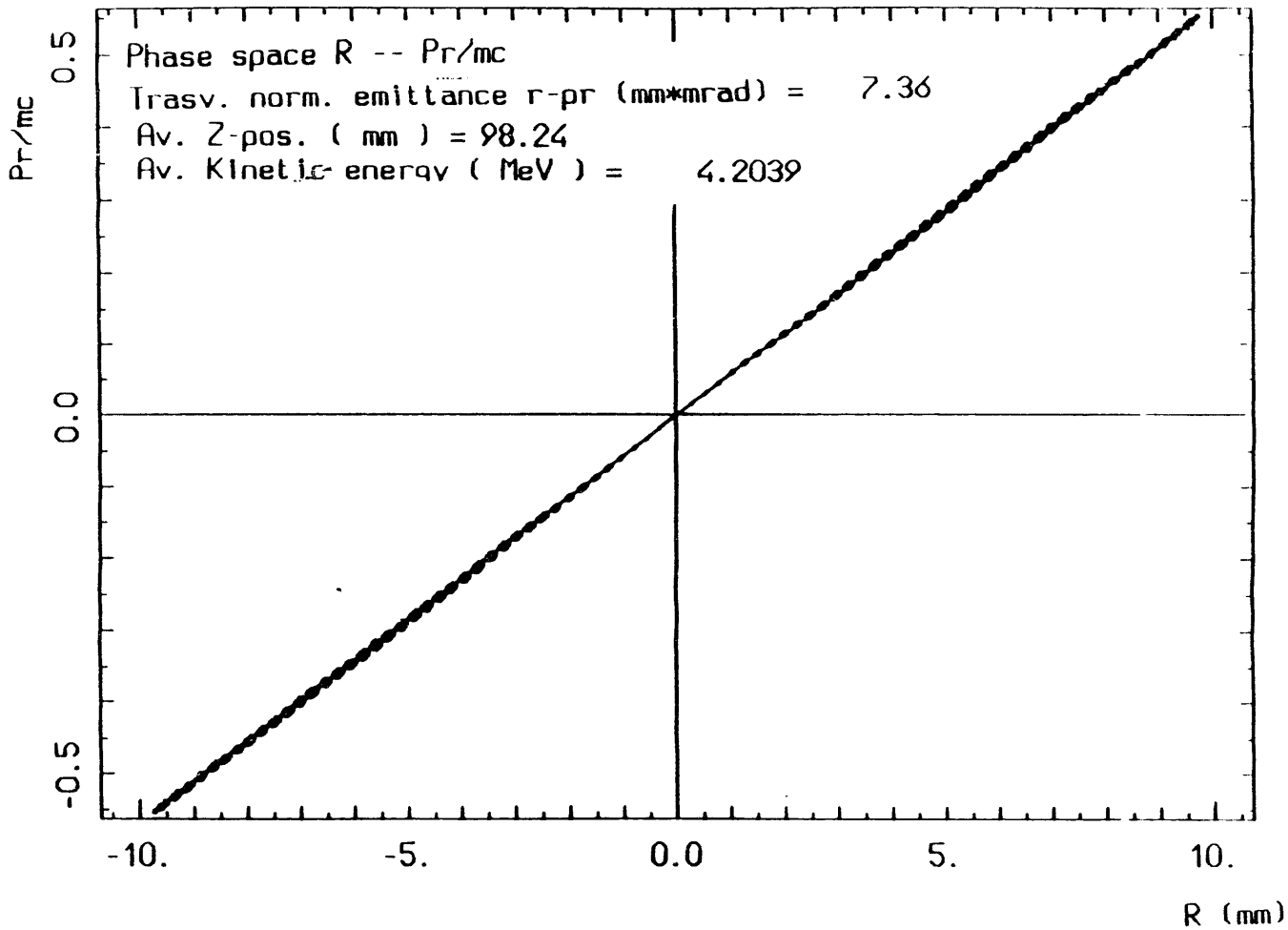

Figure I-12 shows plot of Pr/mc vs R.

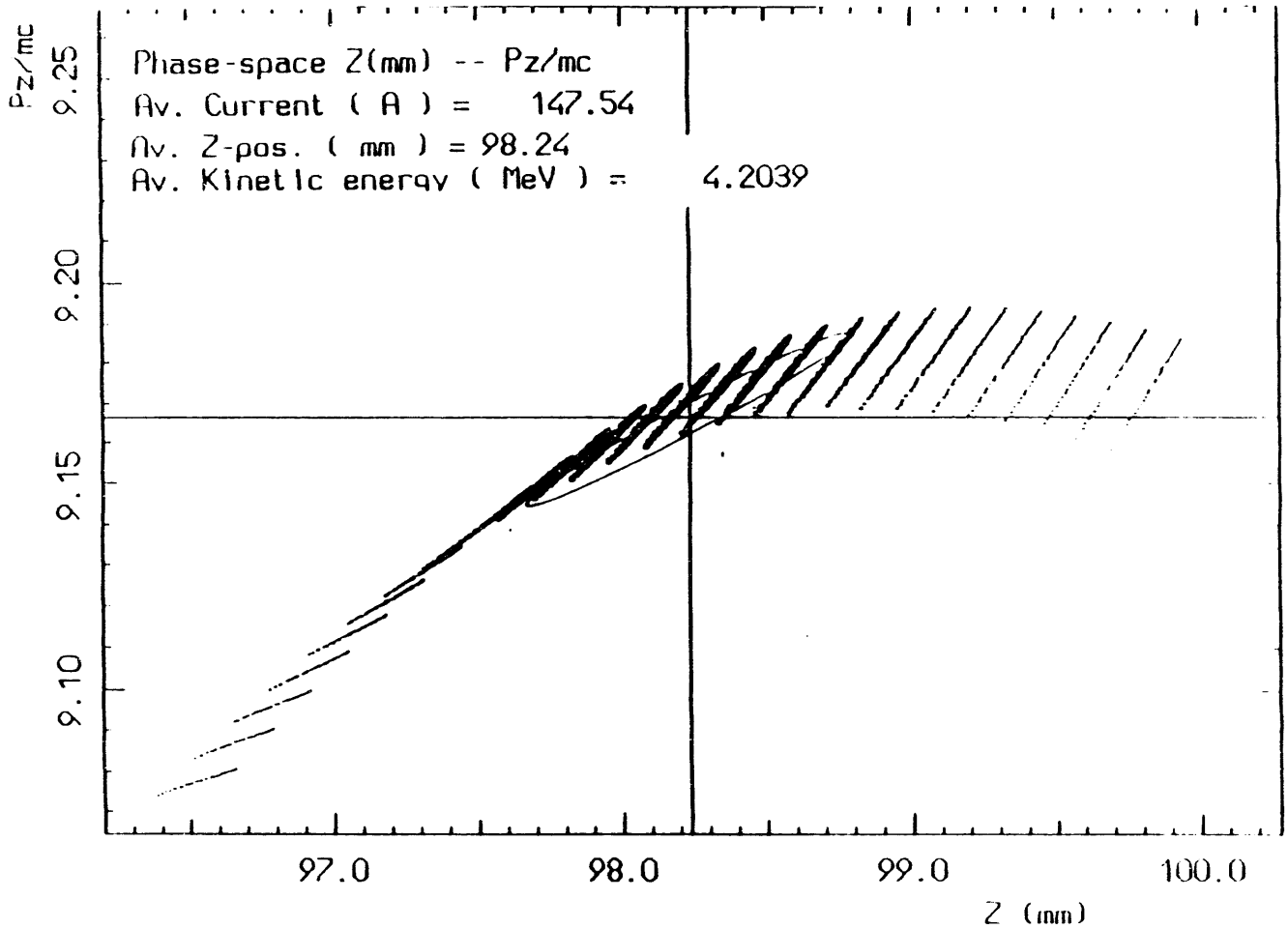

Figure I–14 shows plot of Pz/mc vs z. The solid line is the rms ellipse.

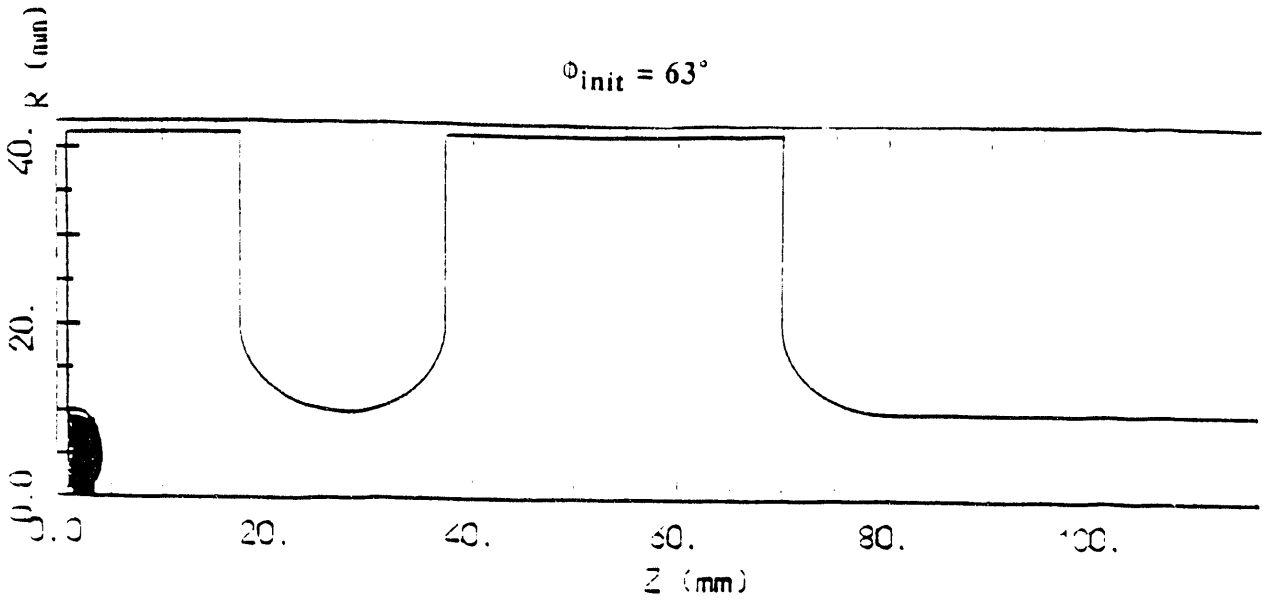

Figure II-1 shows plot of the $r*H_\phi$ = const lines for 1 nC case, total field.

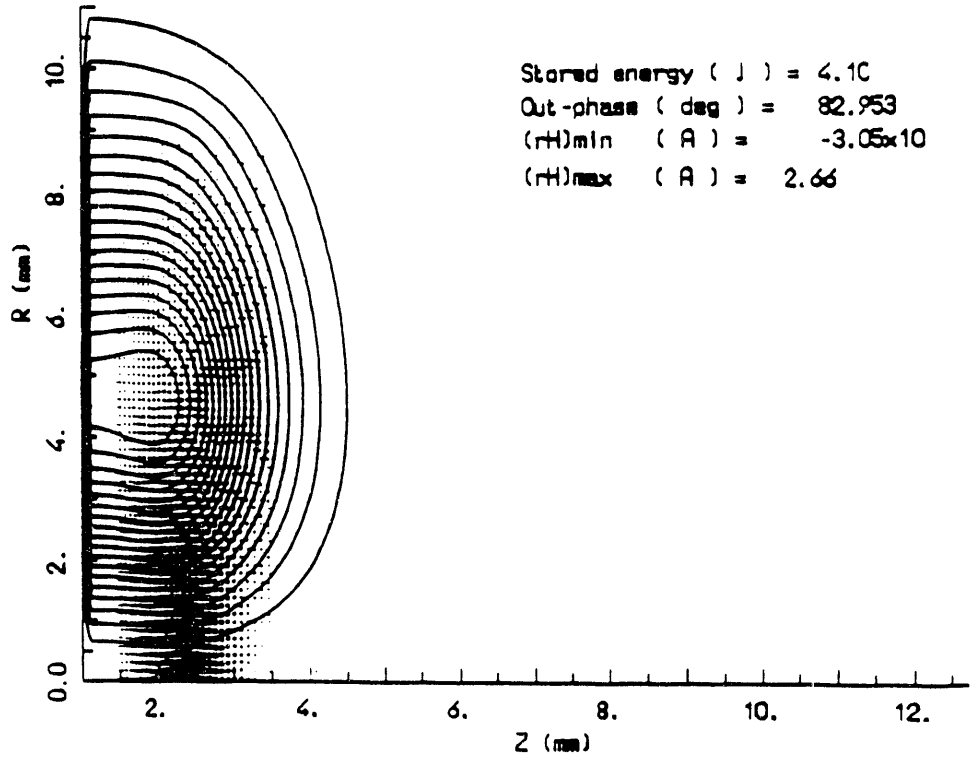

Figure II-2 plot of the lines of self field produced by 1 nC bunch.

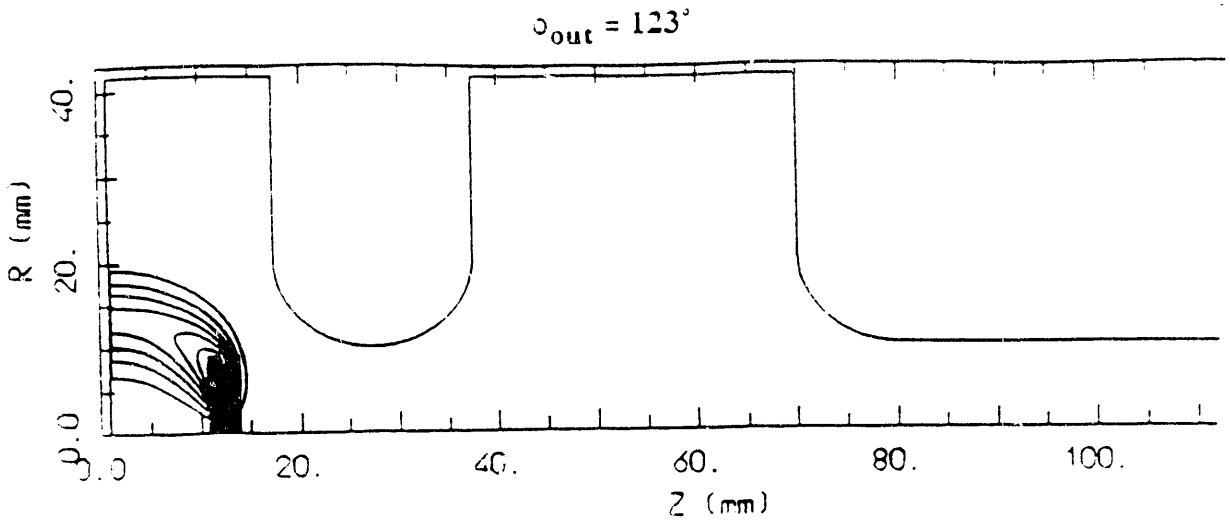

Figure II-5 shows plot of the $r*H_\theta$ = const lines for 1 nC case, total field.

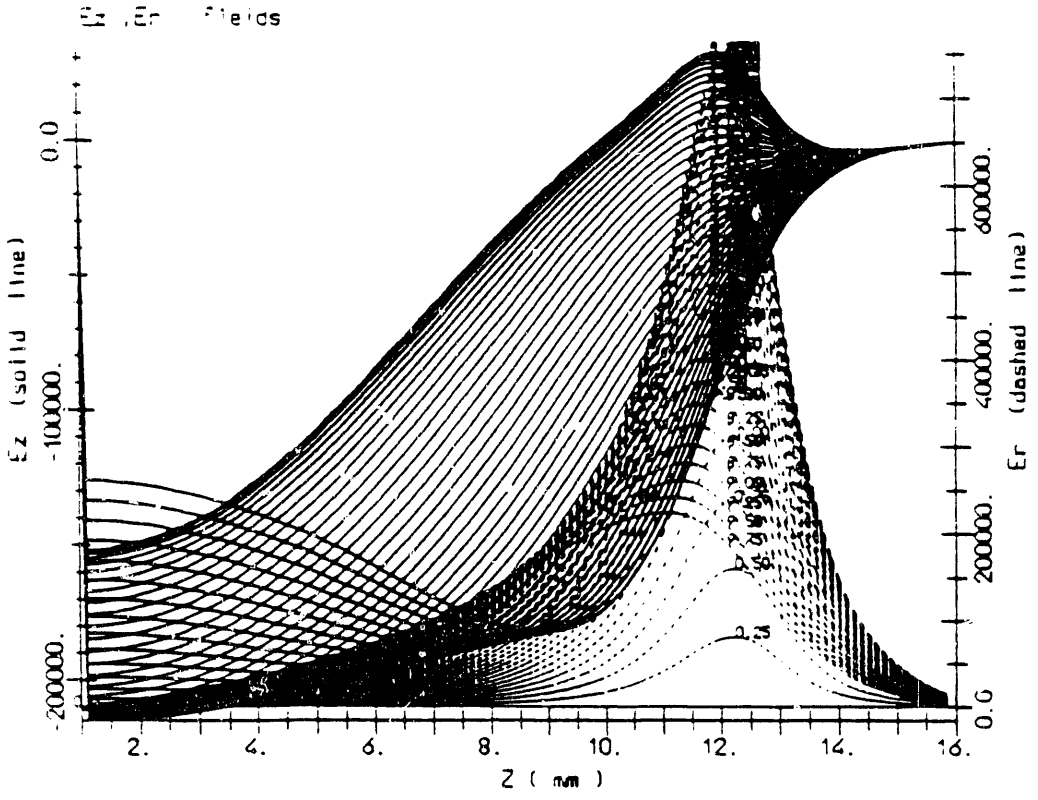

Figure II-6 shows plot of Ez (solid line) and Er (dashed lines) vs Z.

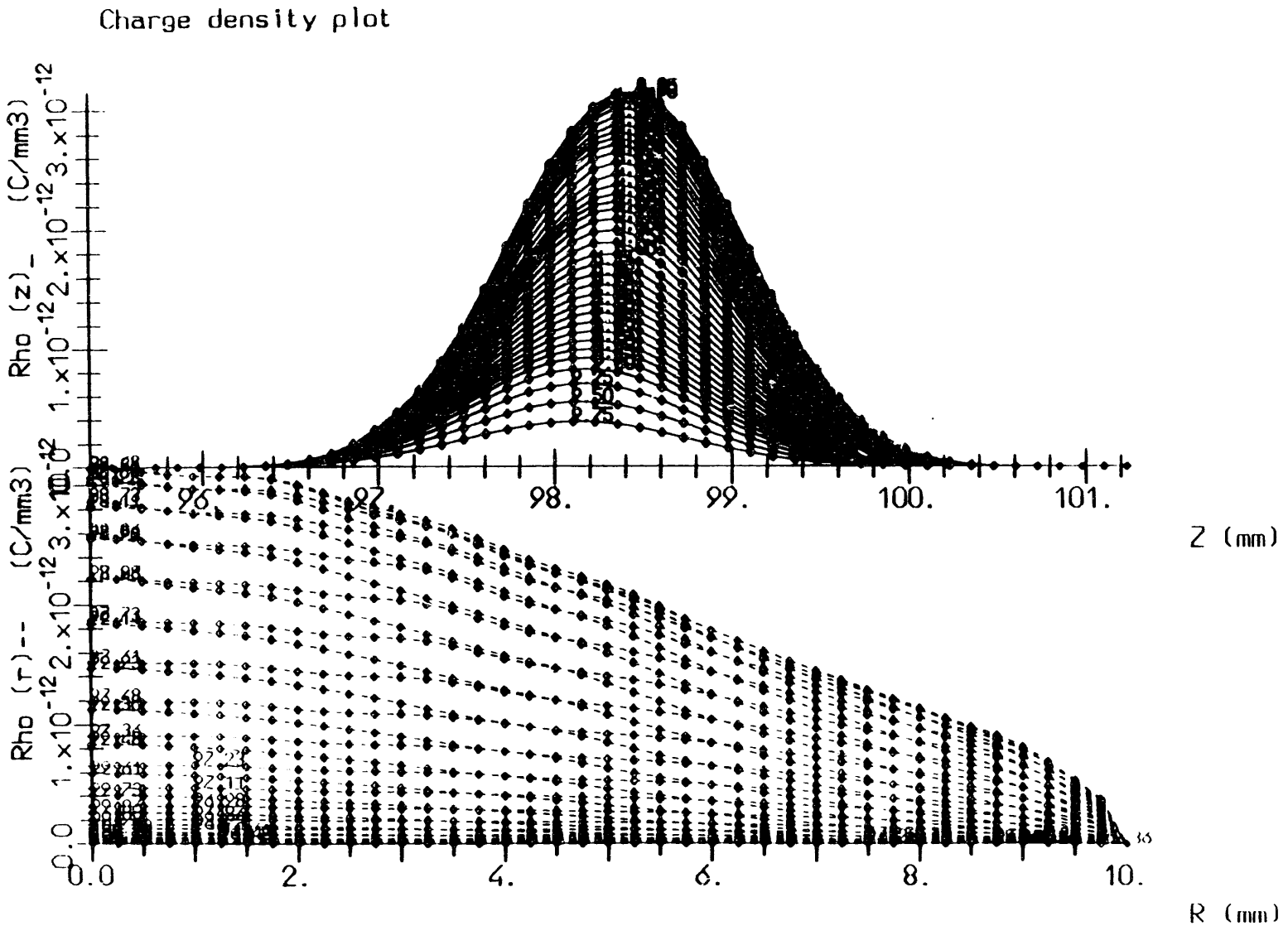

Figure II-9 shows plot of ρ vs z and R.

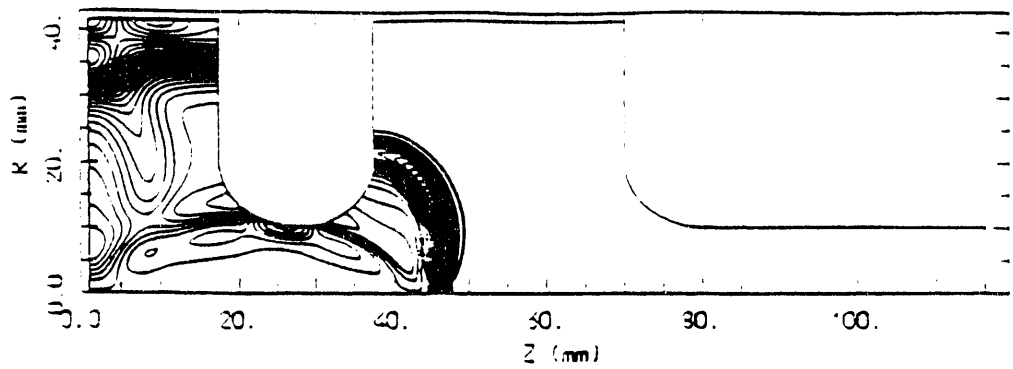

Figure II-11 plot of propagation of the bunch self field produced by the bunch.

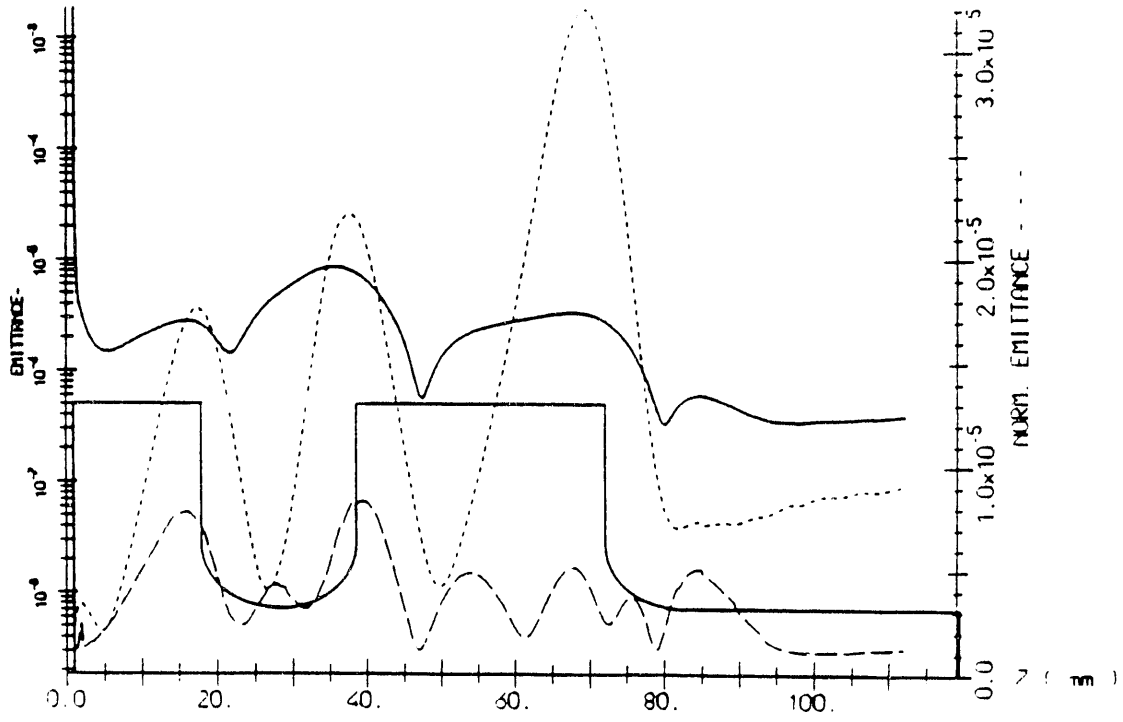

Figure II-12 shows plot of Transverse Emittance vs z. Dashed line shows the normalized emittances $\varepsilon_n = \sqrt{\langle x^2\rangle\langle p_x^2\rangle - \langle xp_x\rangle^2}$; Solid curve line shows the emittance $\varepsilon = \sqrt{\langle x^2\rangle\langle x'^2\rangle - \langle xx'\rangle^2}$ and third curve $\left(\varepsilon_n^{central}\right)$, gives ε_n associated to the central slice of the bunch.

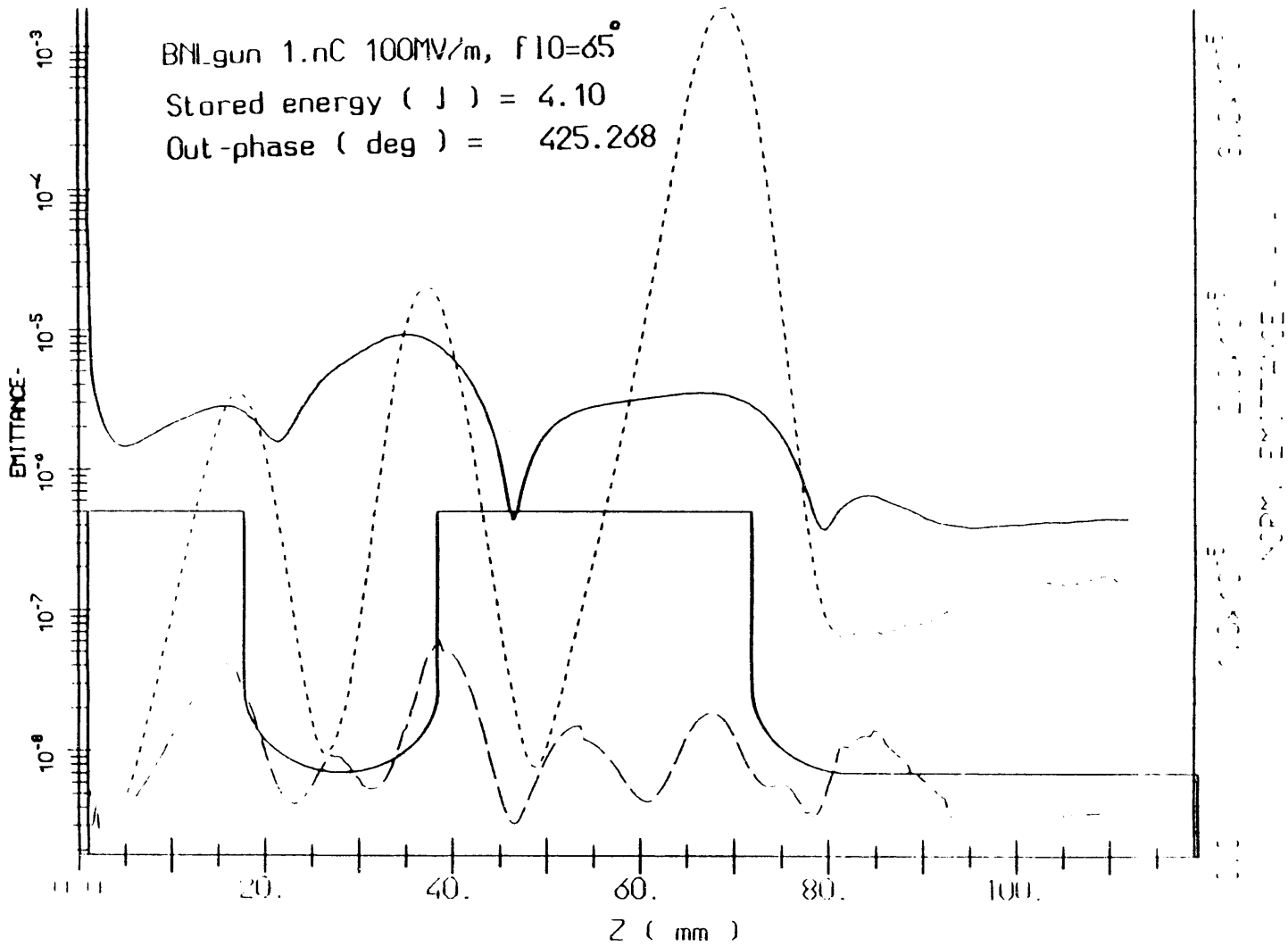

Figure III-3 shows plot of Transverse Emittance vs z. Dashed line shows the normalized emittances $\varepsilon_n = \sqrt{\langle x^2\rangle\langle p_x^2\rangle - \langle x p_x\rangle^2}$; Solid curve line shows the emittance $\varepsilon = \sqrt{\langle x^2\rangle\langle x'^2\rangle - \langle x x'\rangle^2}$ and third curve $\left(\varepsilon_n^{central}\right)$, gives ε_n associated to the central slice of the bunch

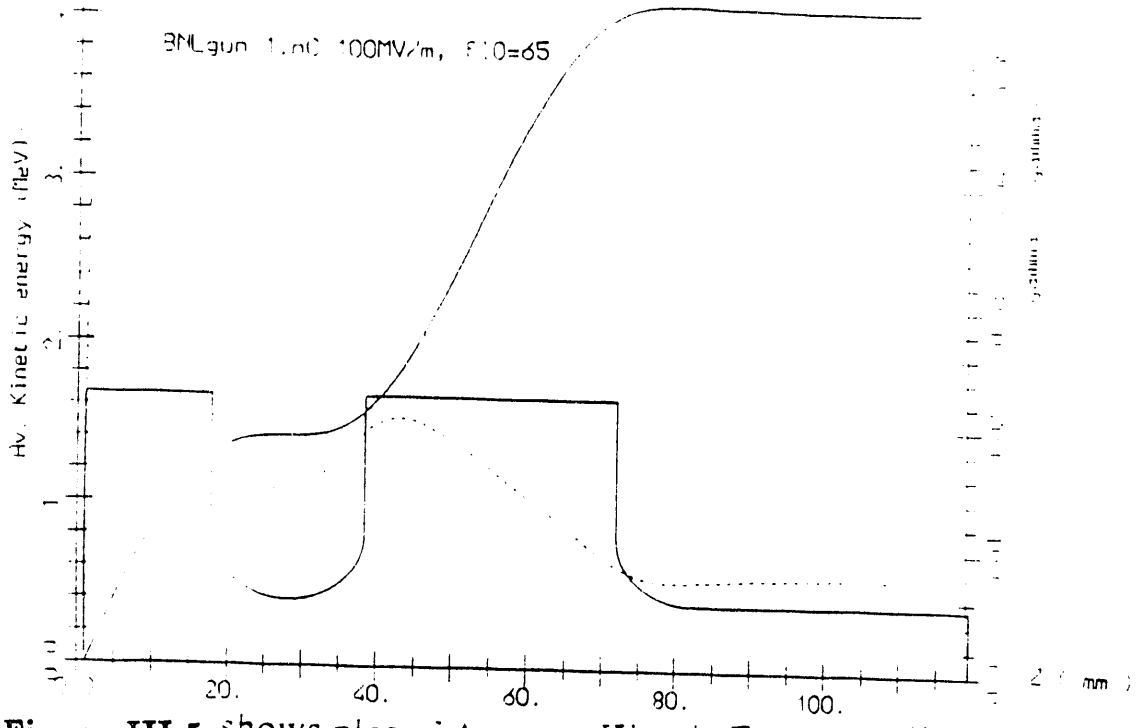

Figure III-5 shows plot of Average Kinetic Energy (solid line) and $\Delta\gamma/\langle\gamma\rangle$ (dashed line), vs z

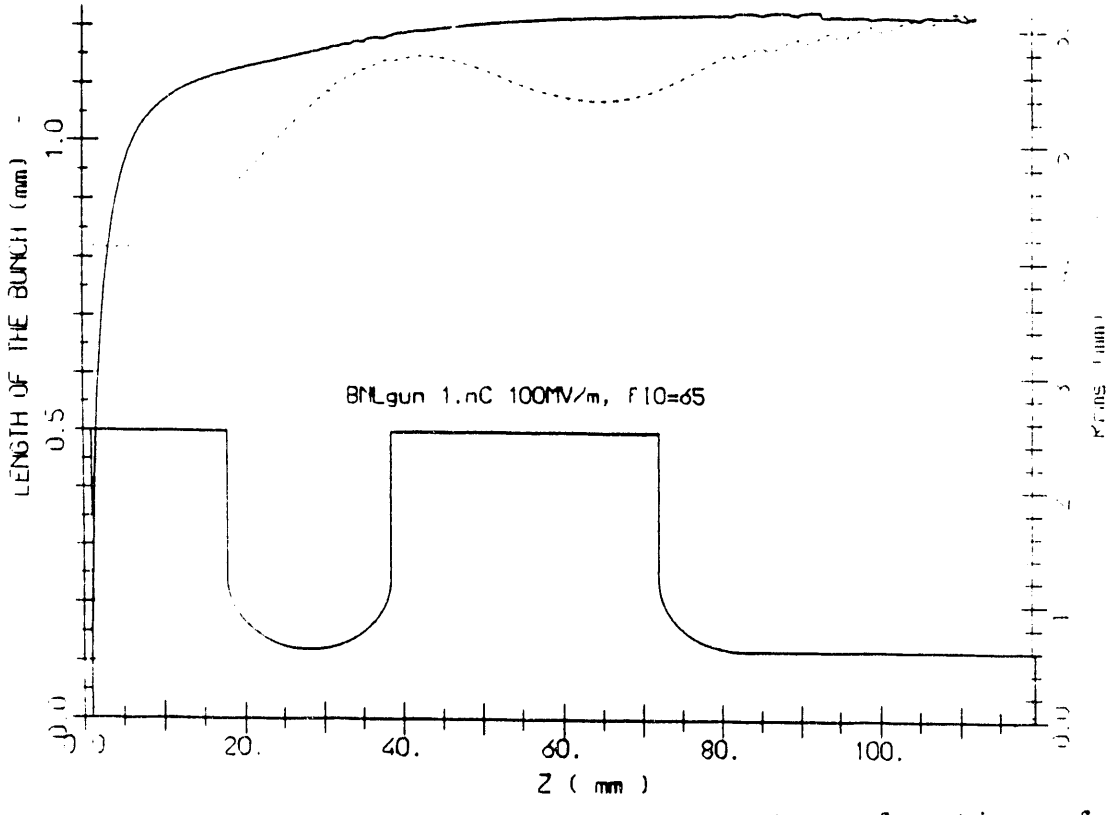

Figure III-6 Plot of length of the bunch as function of z.

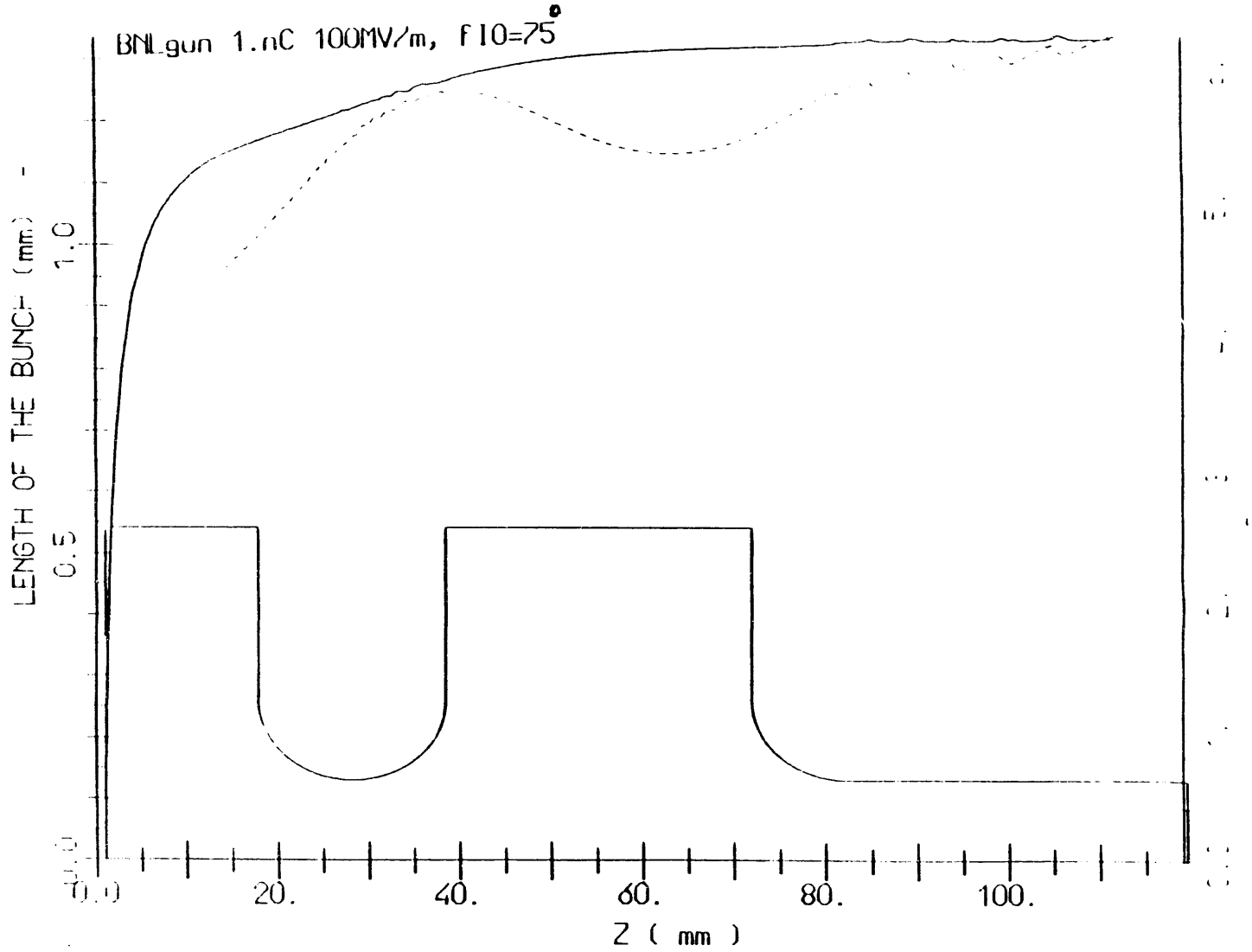

Figure IV-3 Plot of length of the bunch as function of z.

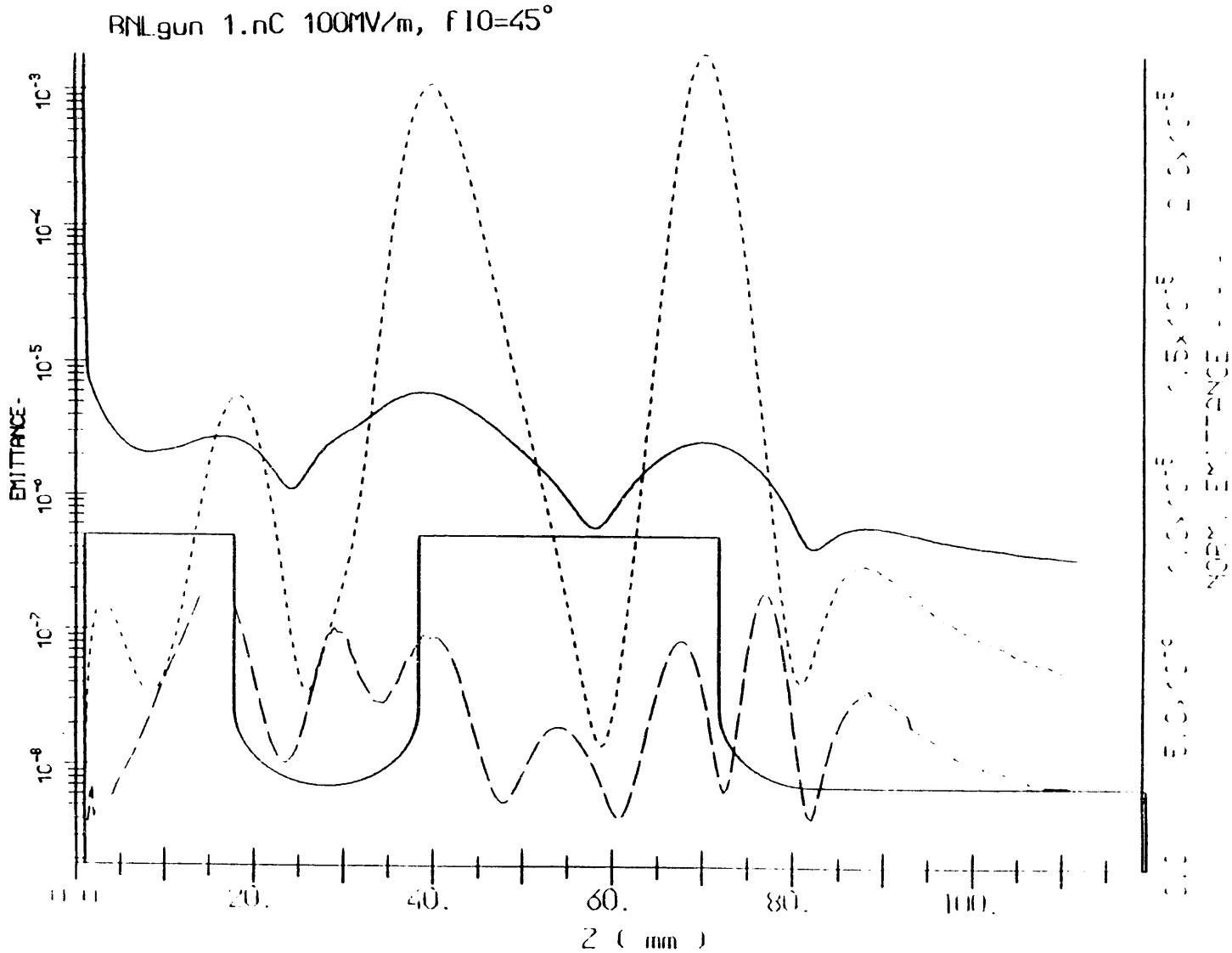

Figure V-3 shows plot of Transverse Emittance vs z. Dashed line shows the normalized emittances $\varepsilon_n = \sqrt{\langle x^2\rangle\langle p_x^2\rangle - \langle x p_x\rangle^2}$; Solid curve line shows the emittance $\varepsilon = \sqrt{\langle x^2\rangle\langle x'^2\rangle - \langle x x'\rangle^2}$ and third curve $\left(\varepsilon_n^{central}\right)$, gives ε_n associated to the central slice of the bunch

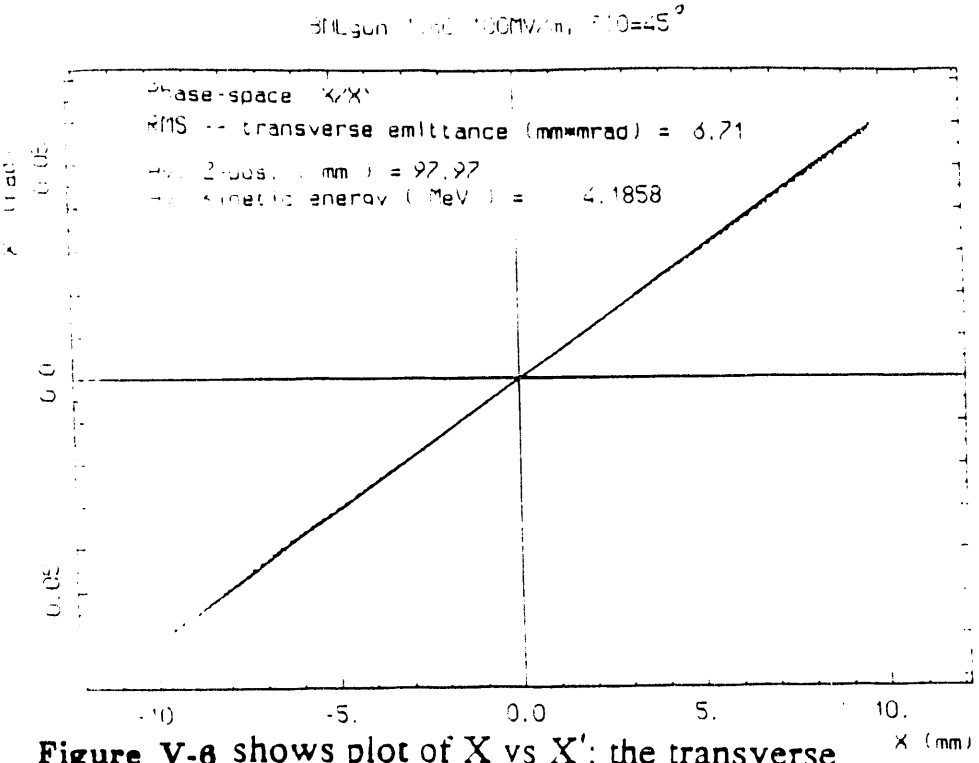

Figure V-6 shows plot of X vs X'; the transverse phase space.

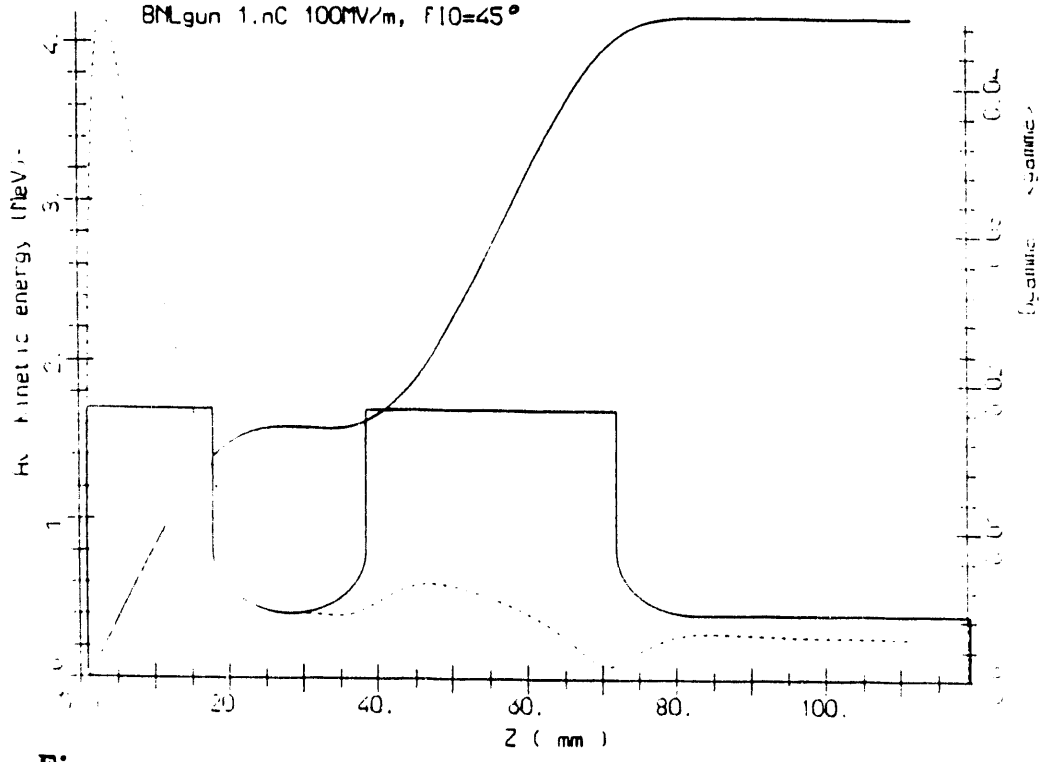

Figure V-7 shows plot of Average Kinetic Energy (solid line) and $\Delta\gamma/\langle\gamma\rangle$ (dashed line), vs z.

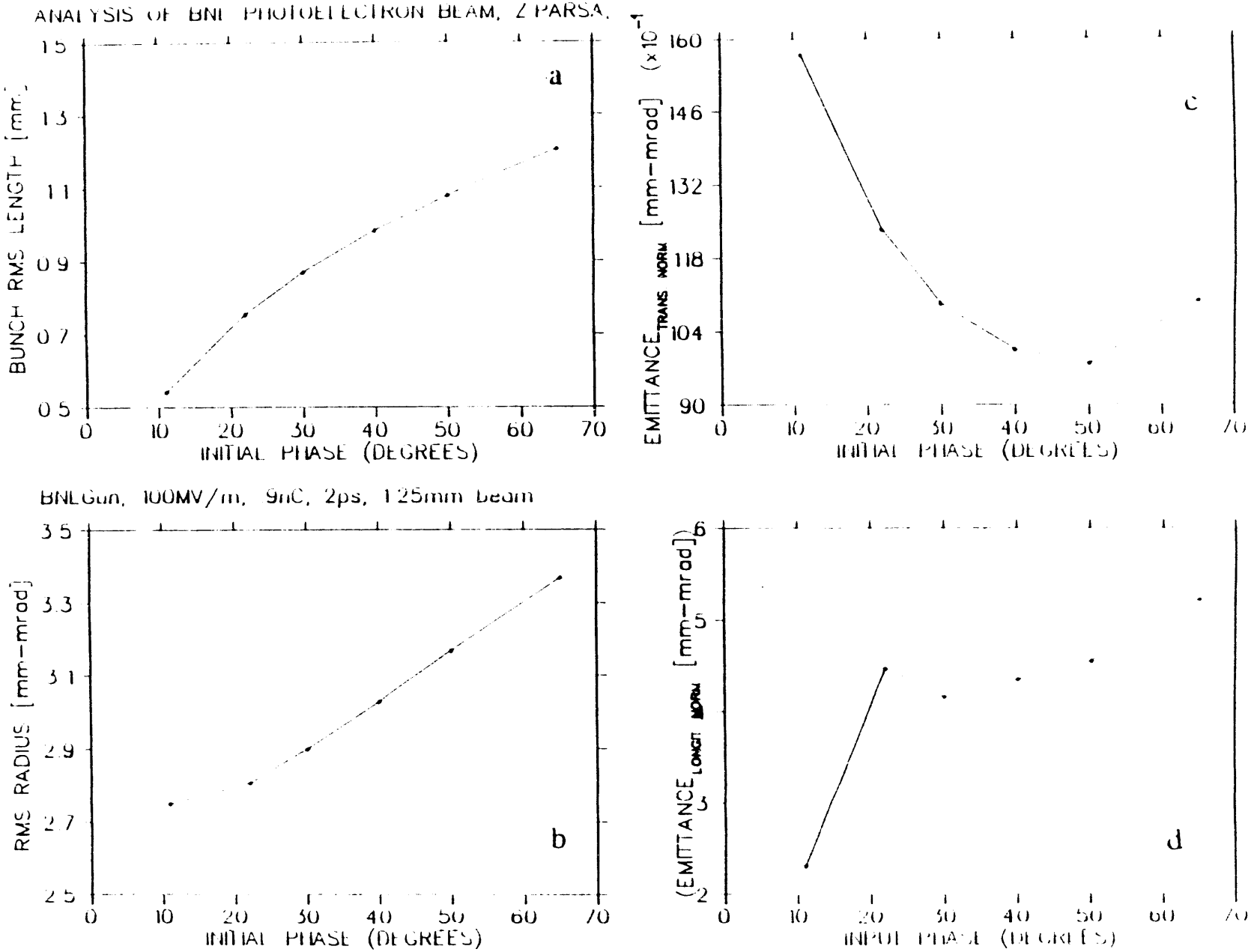

Figure VII-1 a) Variations in the bunch RMS length; b) RMS radius, c) normalized transverse, and d) normalized longitudinal emittance respectively, with respect to variation in the initial phase angle

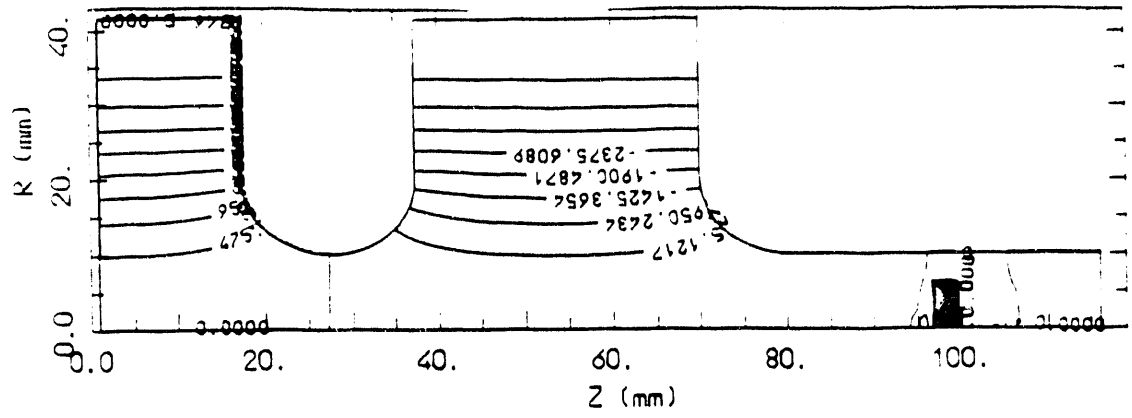

Figure VII-3 shows plot of the $r*H_\phi$ = const lines for 0.3 nC case

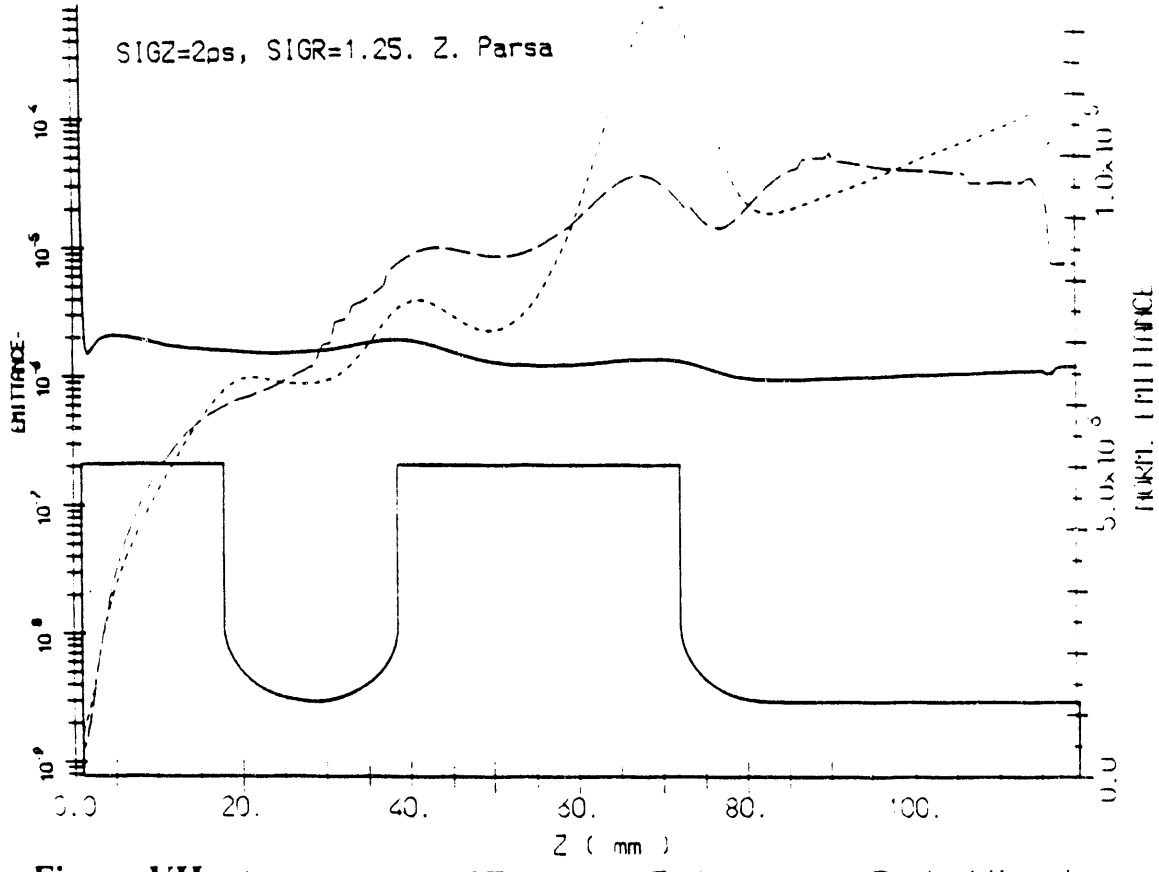

Figure VII-4 shows plot of Transverse Emittance vs z. Dashed line shows the normalized emittances $\varepsilon_n = \gamma\sqrt{\langle x^2\rangle\langle p_x^2\rangle - \langle xp_x\rangle^2}$; Solid curve line shows the emittance $\varepsilon = \gamma\sqrt{\langle x^2\rangle\langle x'^2\rangle - \langle xx'\rangle^2}$ and third curve $(\varepsilon_n^{central})$, gives ε_n associated to the central slice of the bunch.

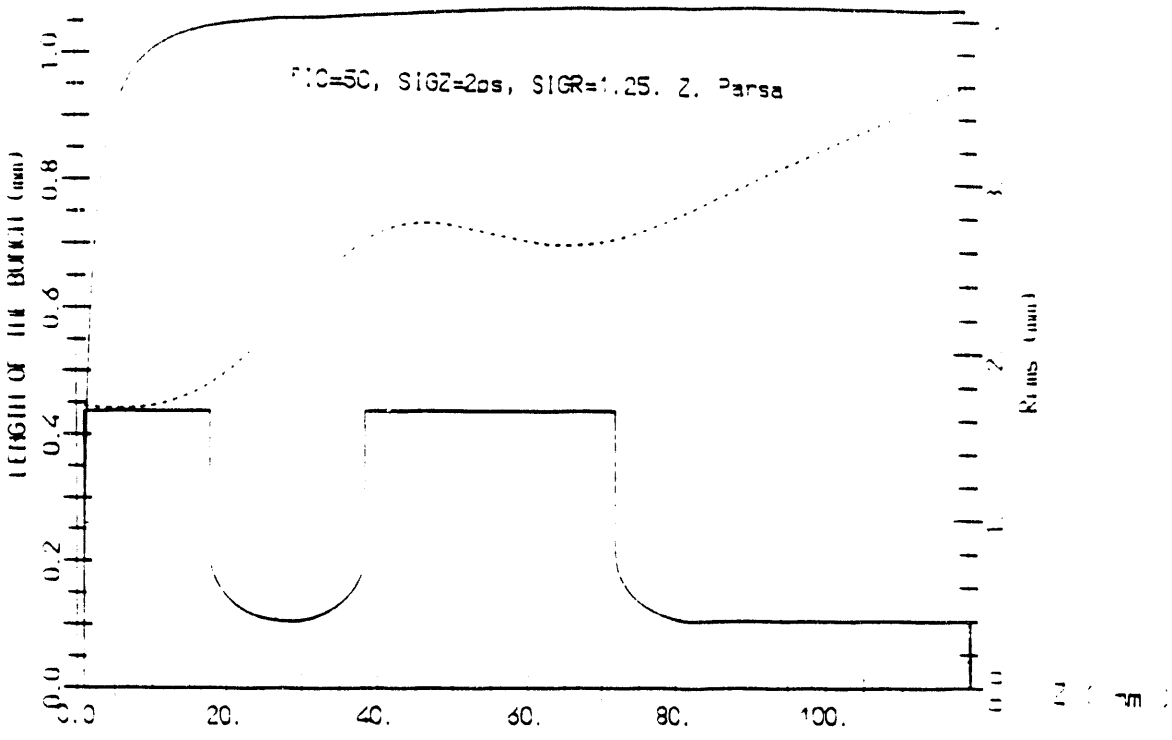

Figure VII-7 shows plot of length of the bunch and Rrms vs z.

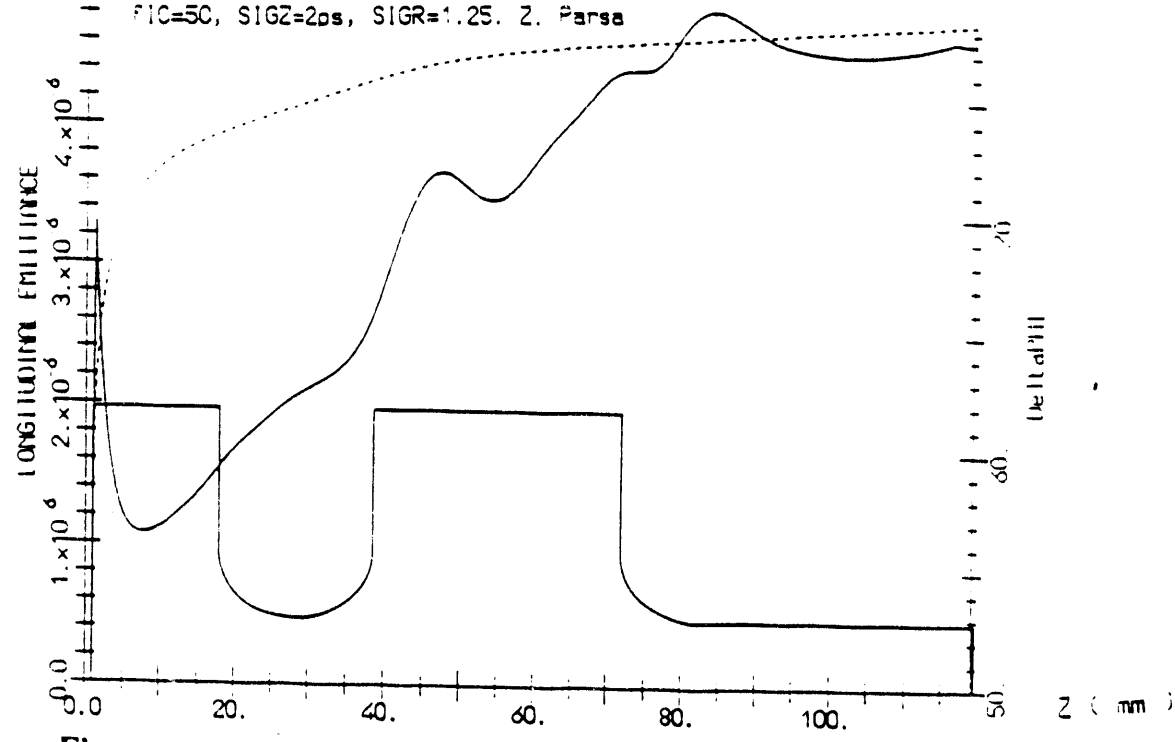

Figure VII- 8 Plot of the longitudinal emittance as function of z

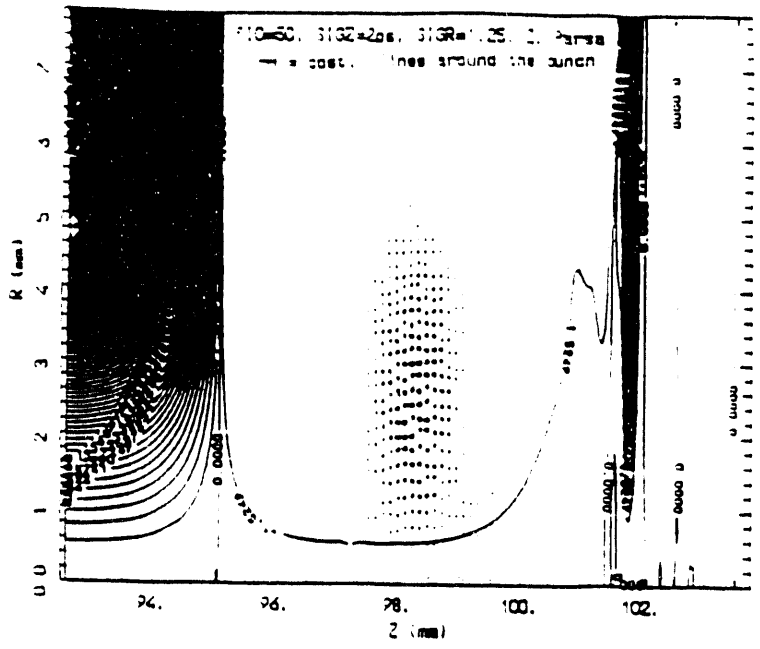

Figure VII-11 snows plot of the $r*H_\theta$ = const lines

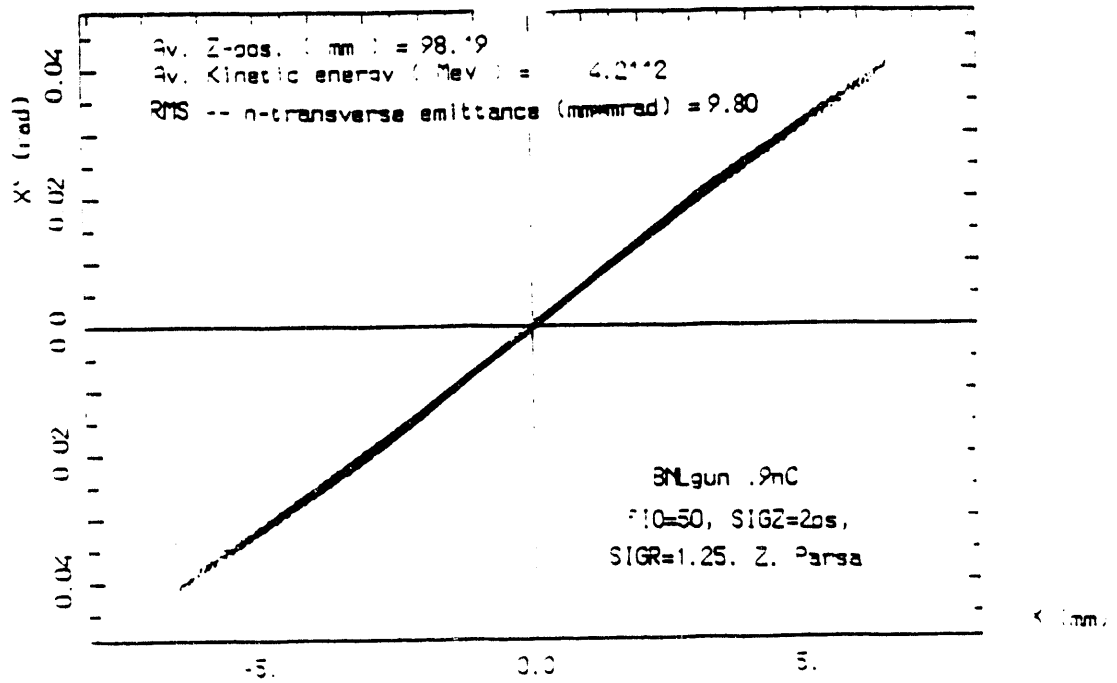

Figure VII-12 shows plot of X vs X'; the transverse phase space.

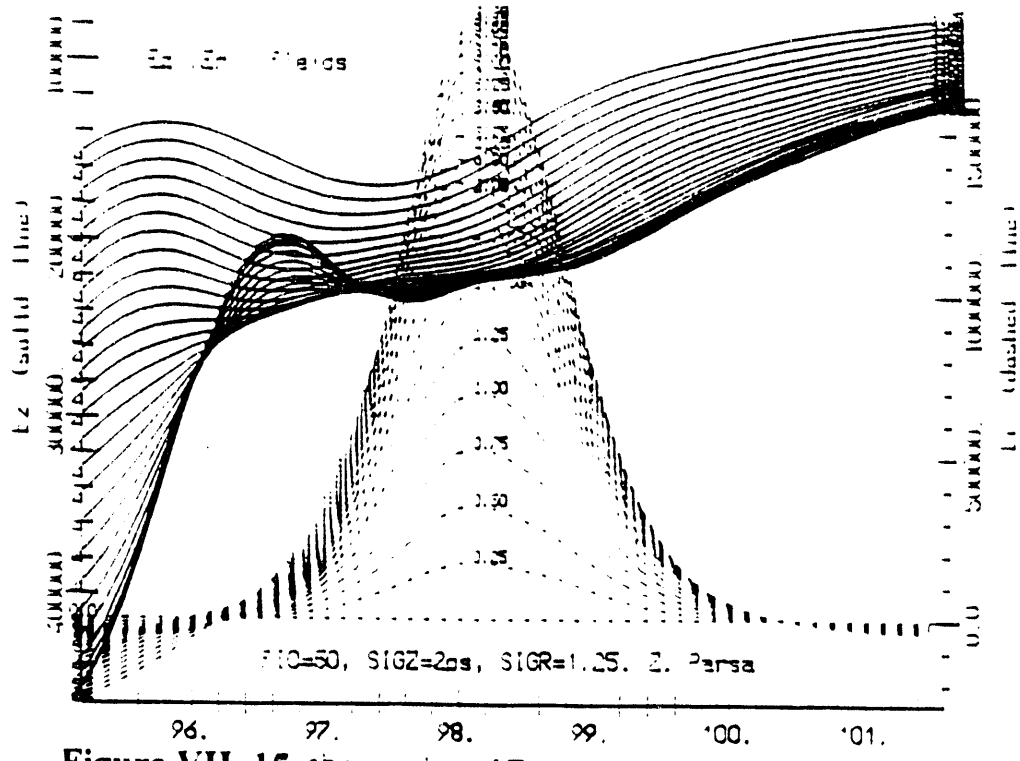

Figure VII- 15 shows plot of Ez (solid line) and Er (dashed lines) vs Z.

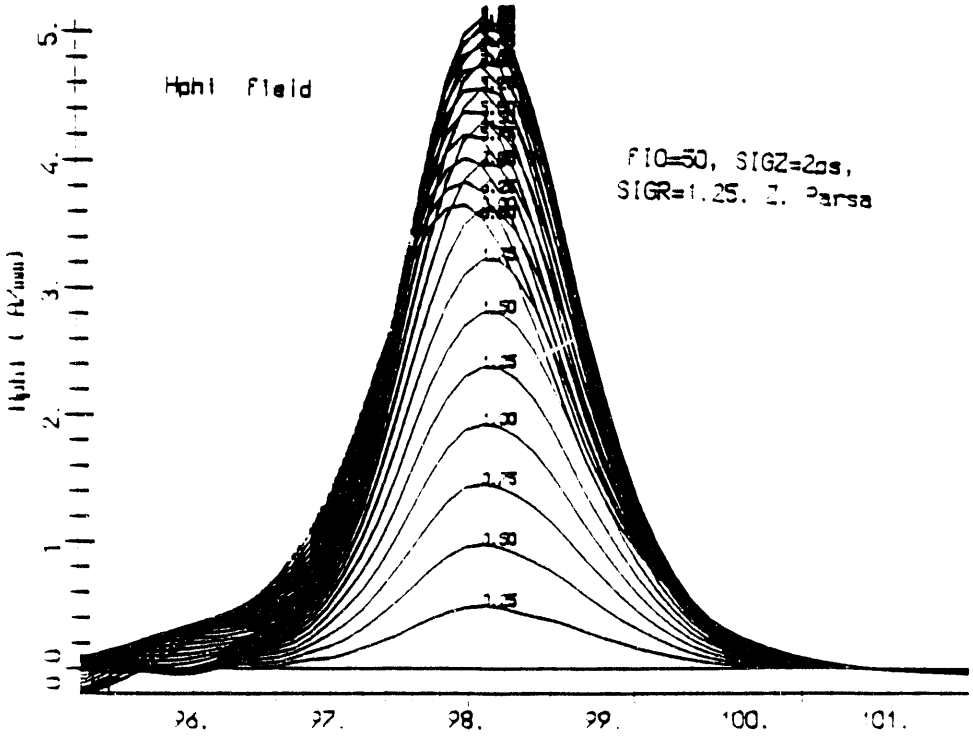

Figure VII- 16 shows plot of the $r*H_\phi$ = const lines for 1 nC case. total field.

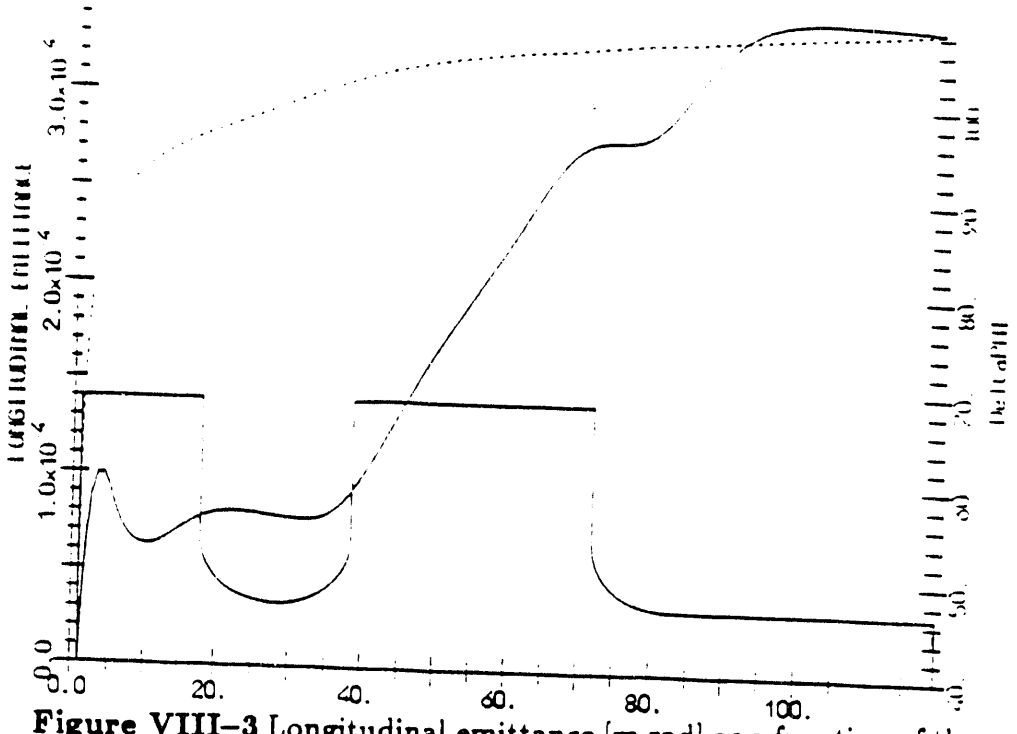

Figure VIII–3 Longitudinal emittance [m rad] as a function of the bunch position z [mm]. The solid line (left scale) shows the normalized rms emittance, and the dashed lines shows $\delta\phi$ (right scale) along the cavity, with $\phi_0 = 40°$, and $E_0 = 62$ Mv/m on the cathode.

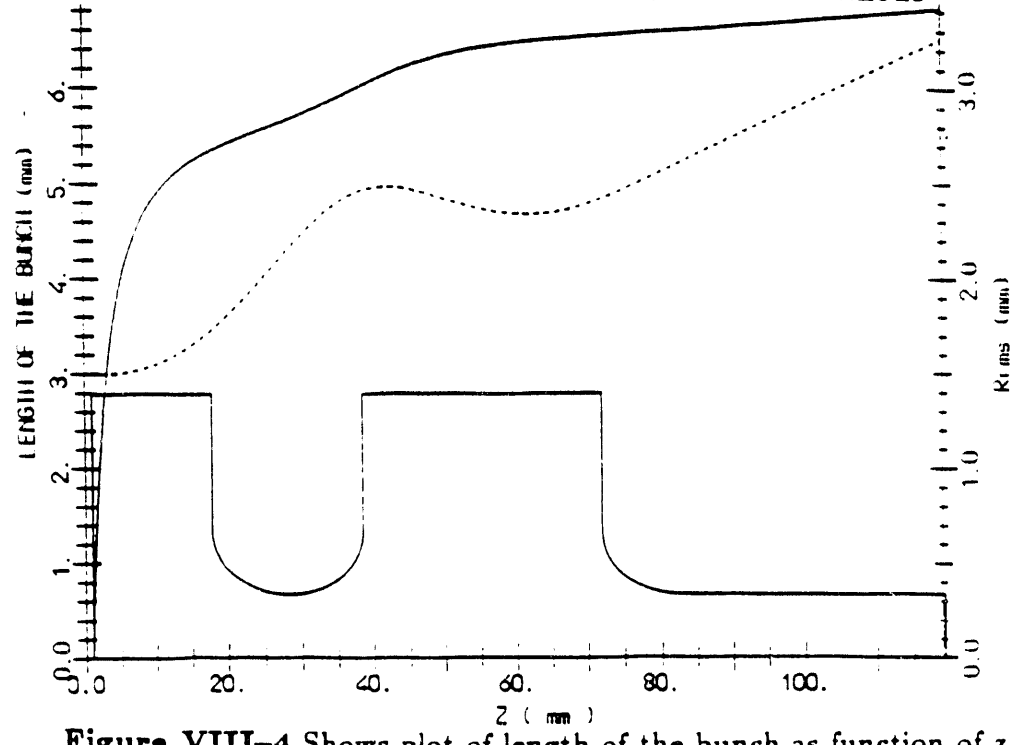

Figure VIII–4 Shows plot of length of the bunch as function of z.

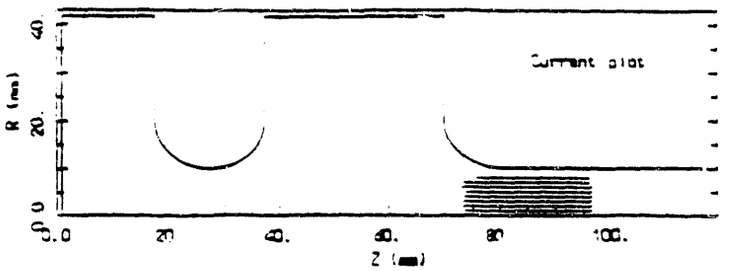

Figure VIII-7 Shows current plot and the location of the particles along the cavity. The boundary of the BNL rf-gun geometry is also given.

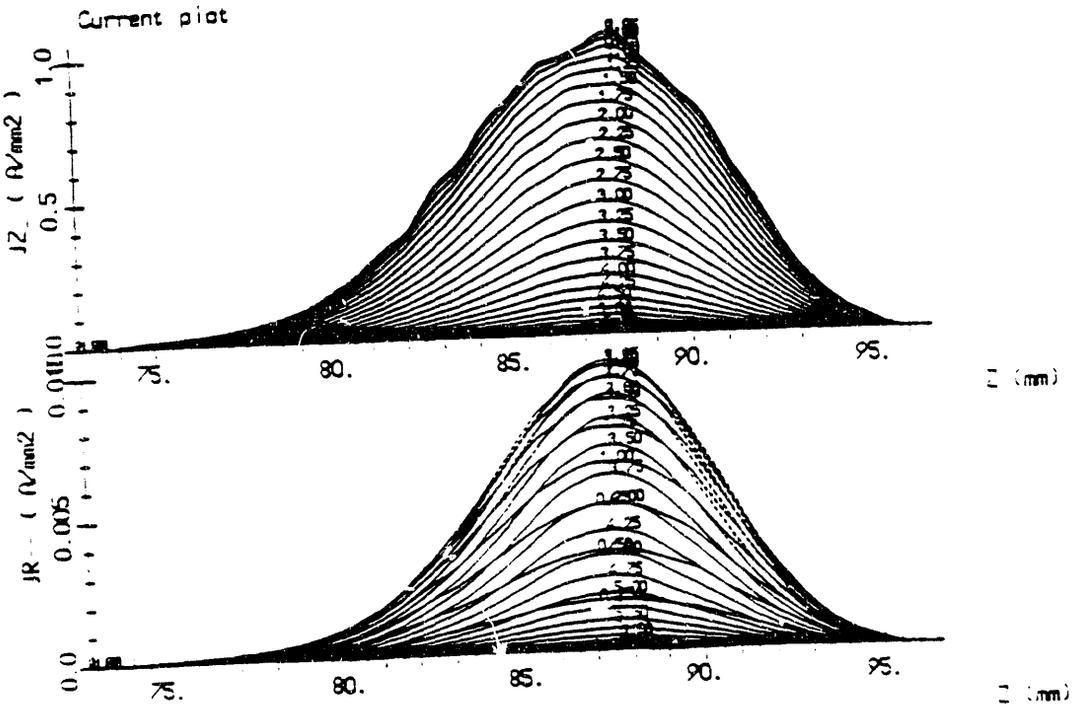

Figure VIII-8 Shows plot of Current density distributions as functions of z at different radii, (see equations in section III).

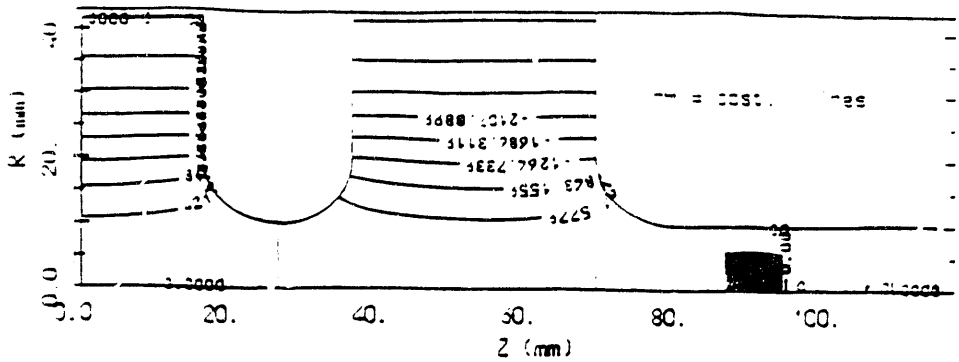

Figure IX–1 Shows plot of the $r * H_\phi = const$ *lines for* $0.9nC$ *and* $5ps$*case*

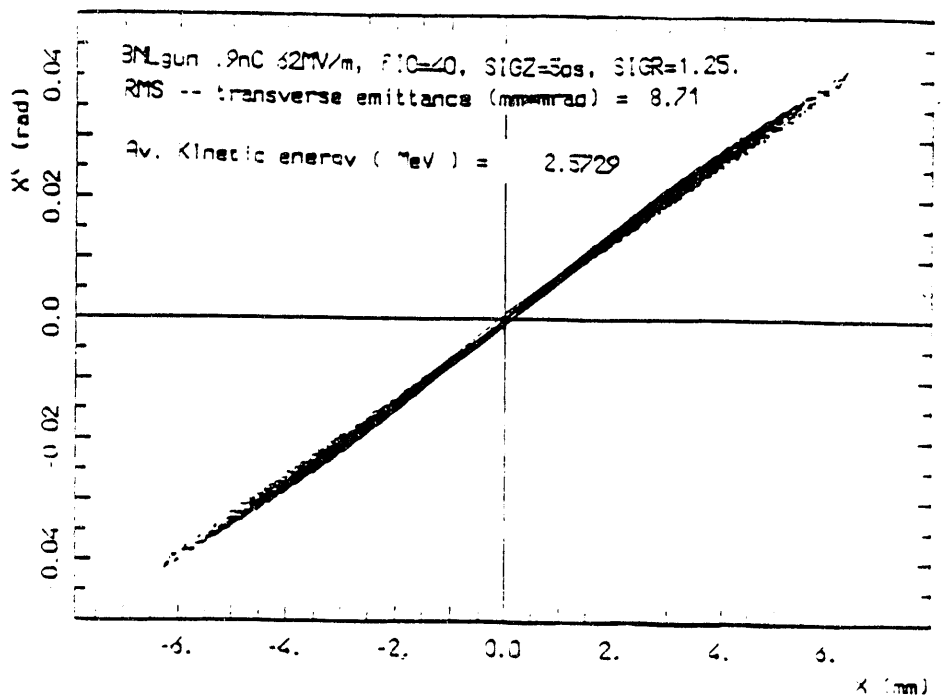

Figure IX–2 Shows plot of X vs X'; the transverse phase space at Average Z = 92.6 mm for .9nC and 5 ps case.

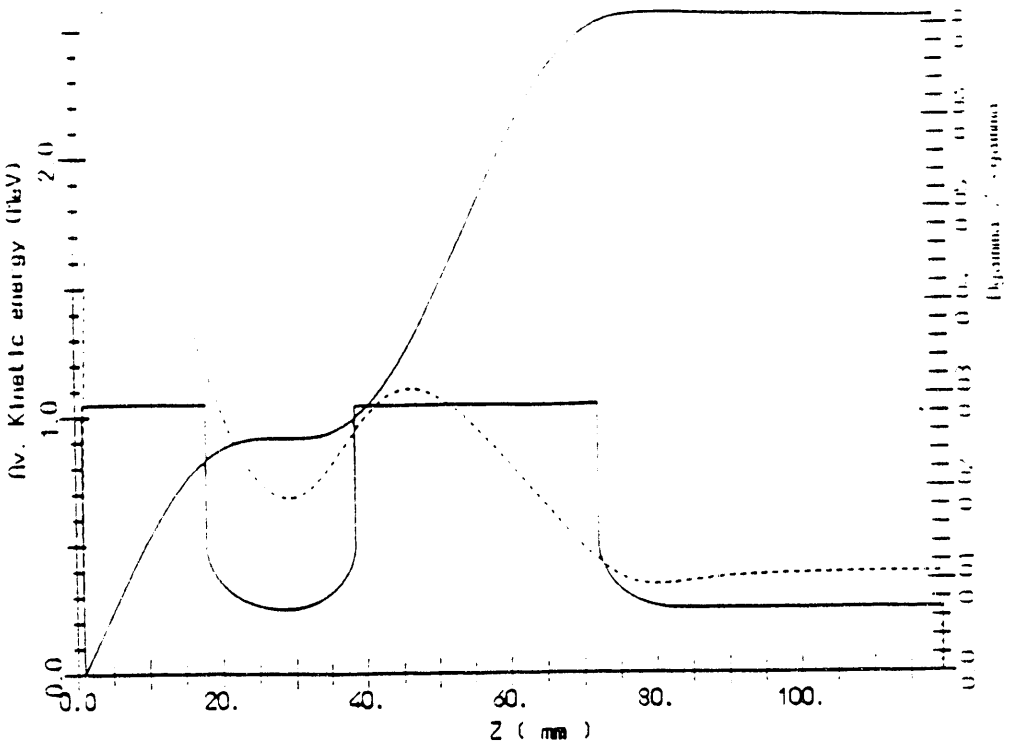

Figure IX–5 Shows plot of Average Kinetic Energy (solid line) vs z.

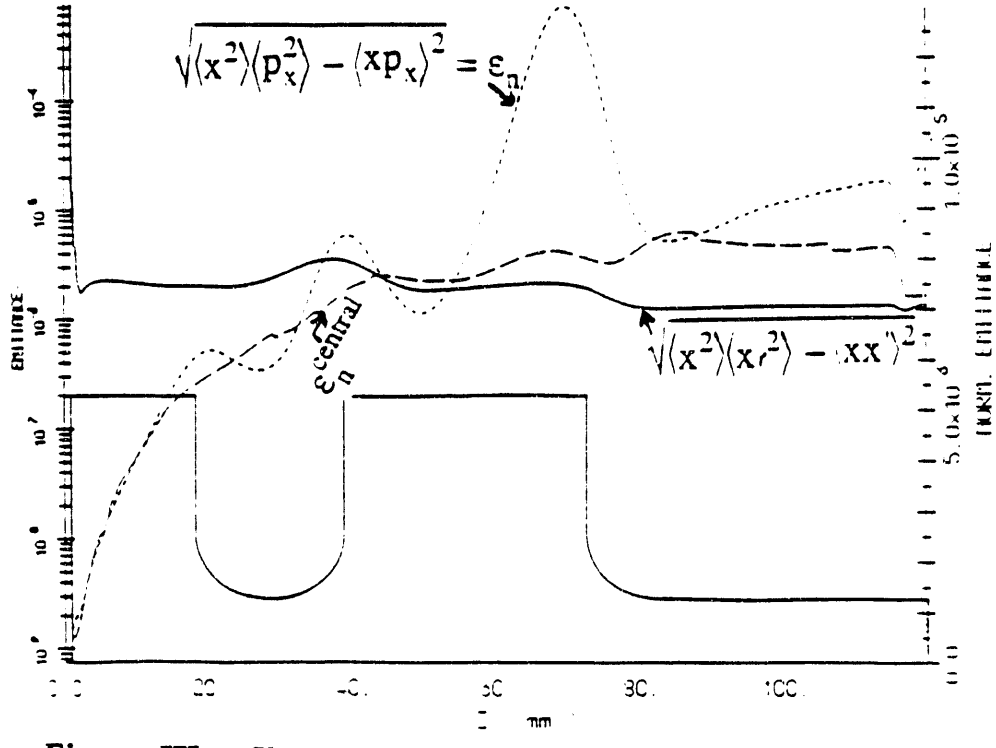

Figure IX–6 Shows plot of Transverse Emittance vs z.

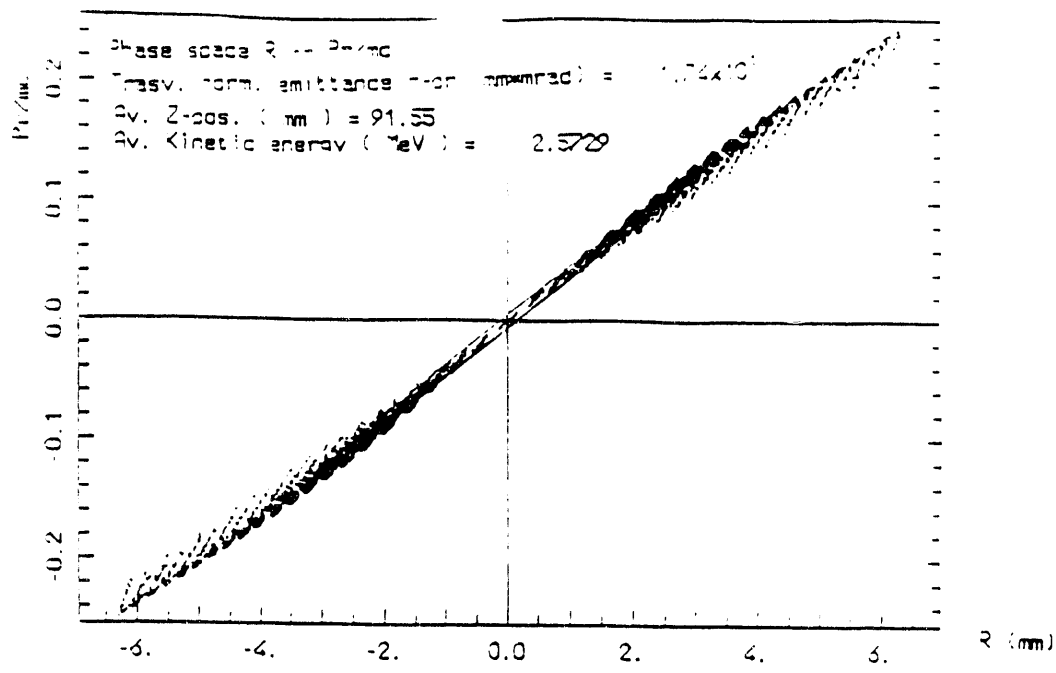

Figure IX–9 Shows plot P_r/mc vs R, (at Average Z = 92 mm). The solid line is the rms ellipse.

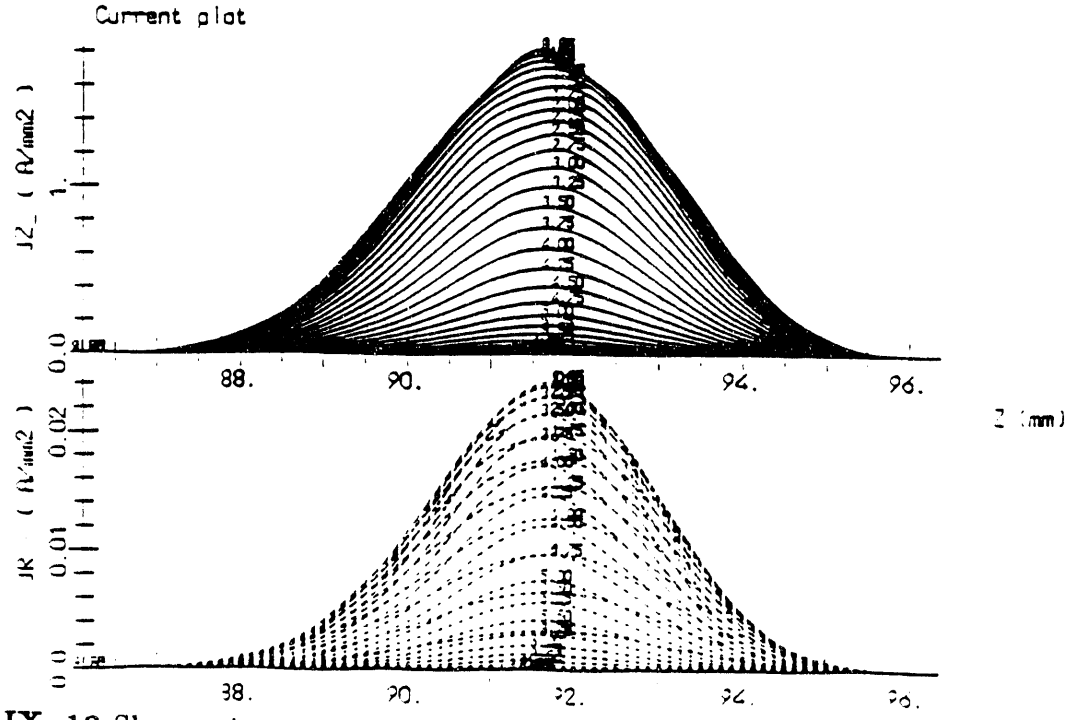

Figure IX–10 Shows plot of Current density distributions as functions of z at different radii.

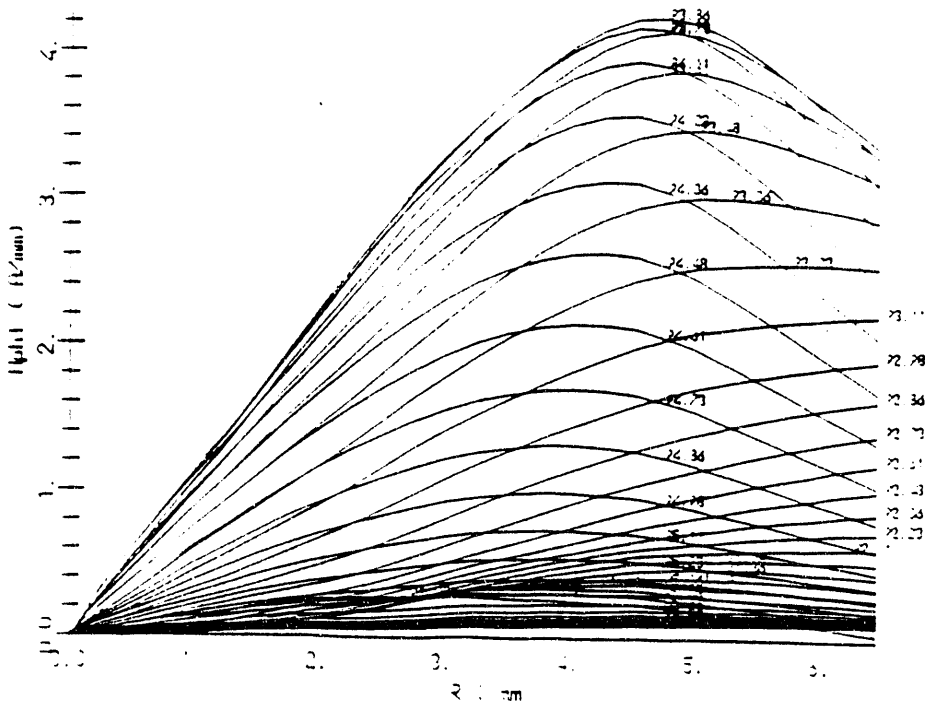

Figure X–3 Shows plot of the H_ϕ vs R. This plot shows the magnetic component of the field.

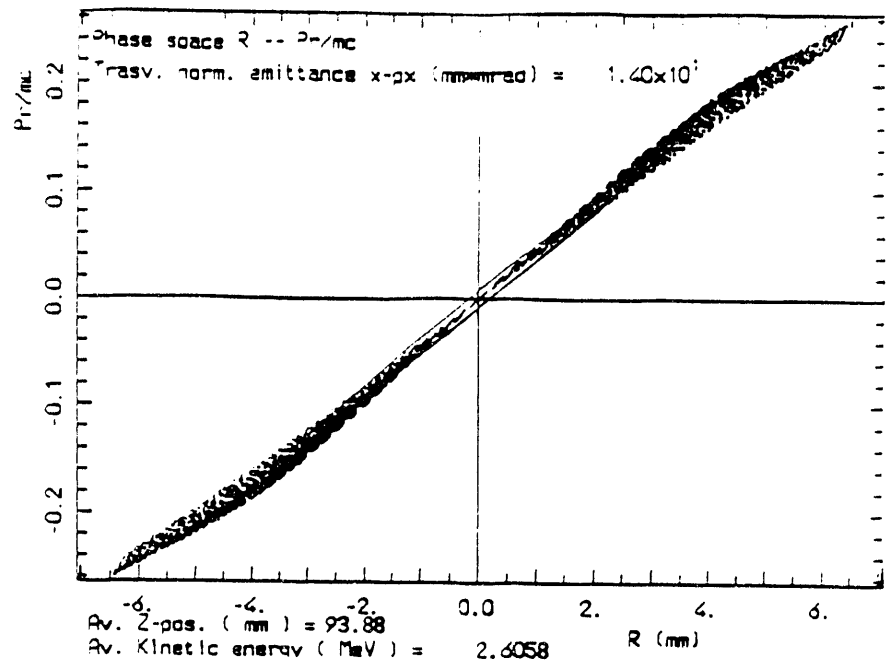

Figure X–4 Shows plot P_r/mc vs R, (at Average Z = 94 mm). The solid line is the rms ellipse.

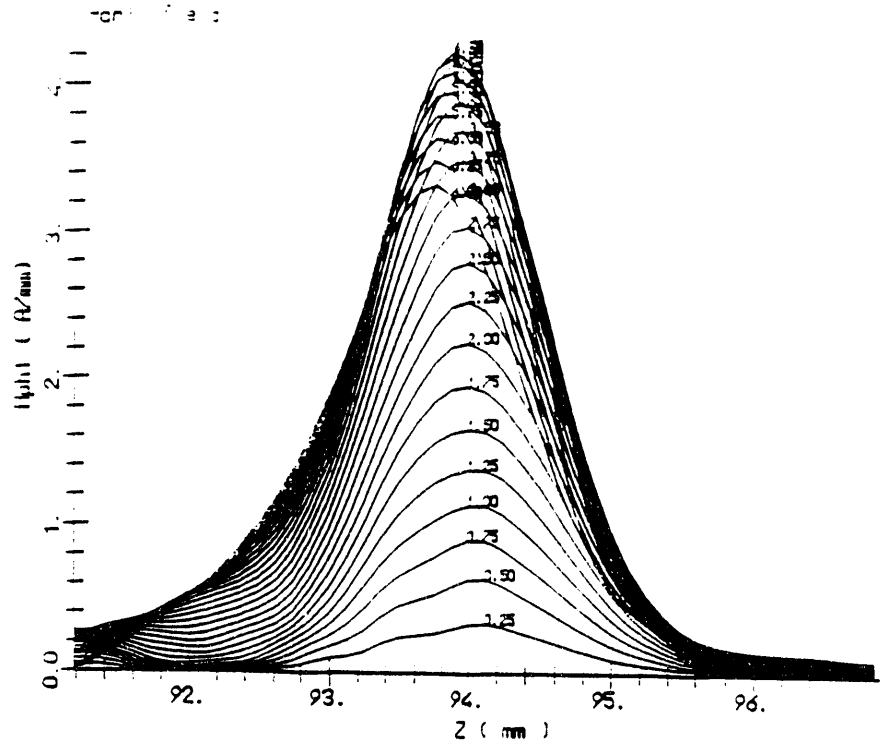

Figure X–7 Shows plot of the H_ϕ vs z. This plot shows the magnetic component of the self-field.

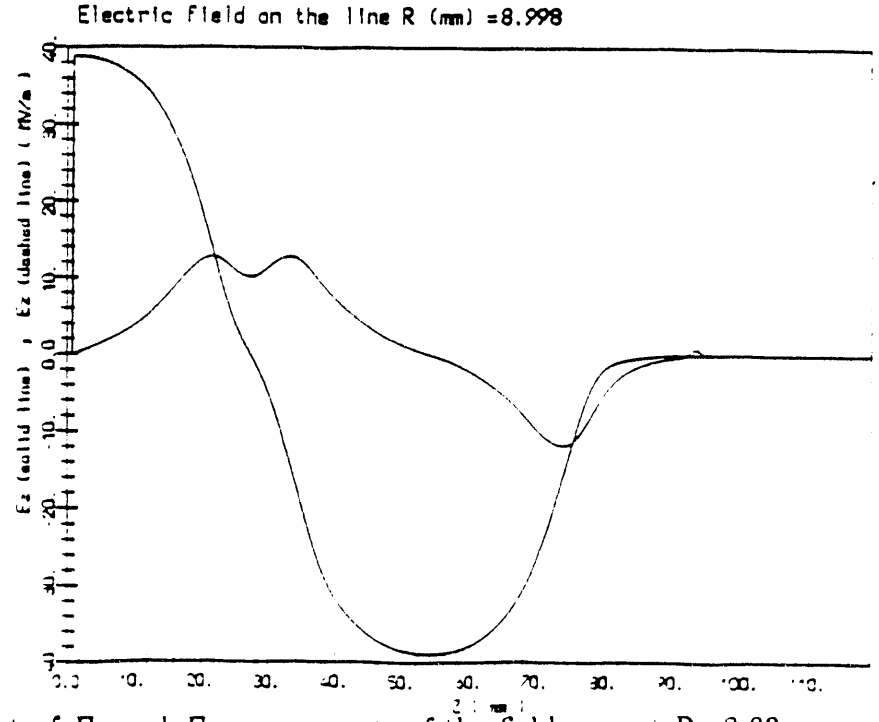

Figure X–8 Shows plot of E_z and E_r components of the field vs z at R=8.99 mm.

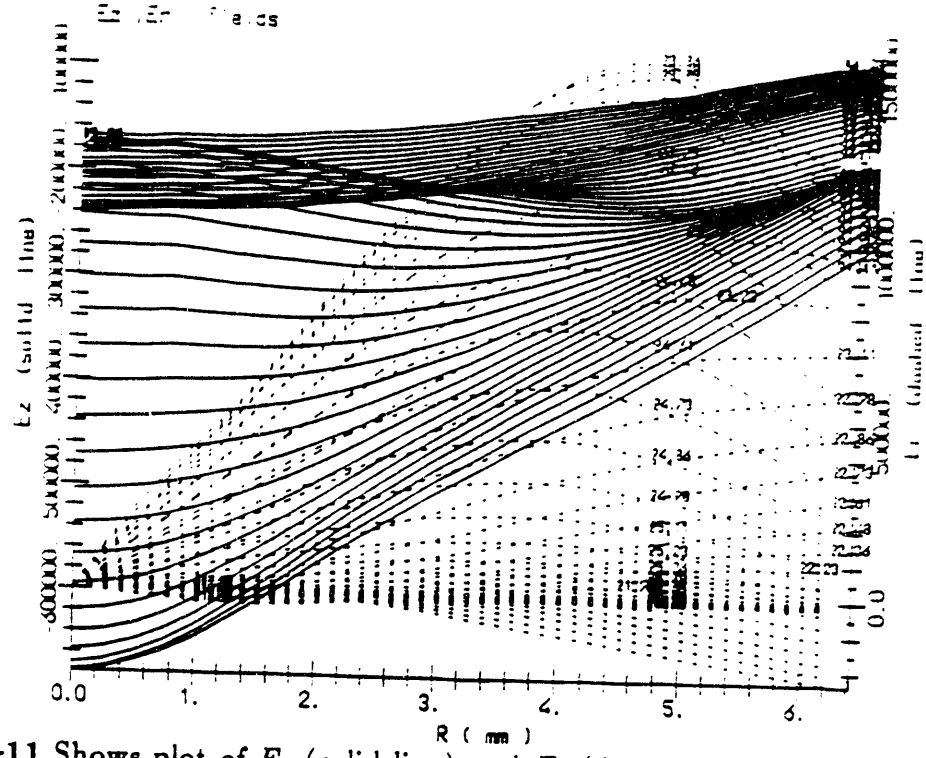

Figure X–11 Shows plot of E_z (solid line) and E_r (dashed lines) vs R.

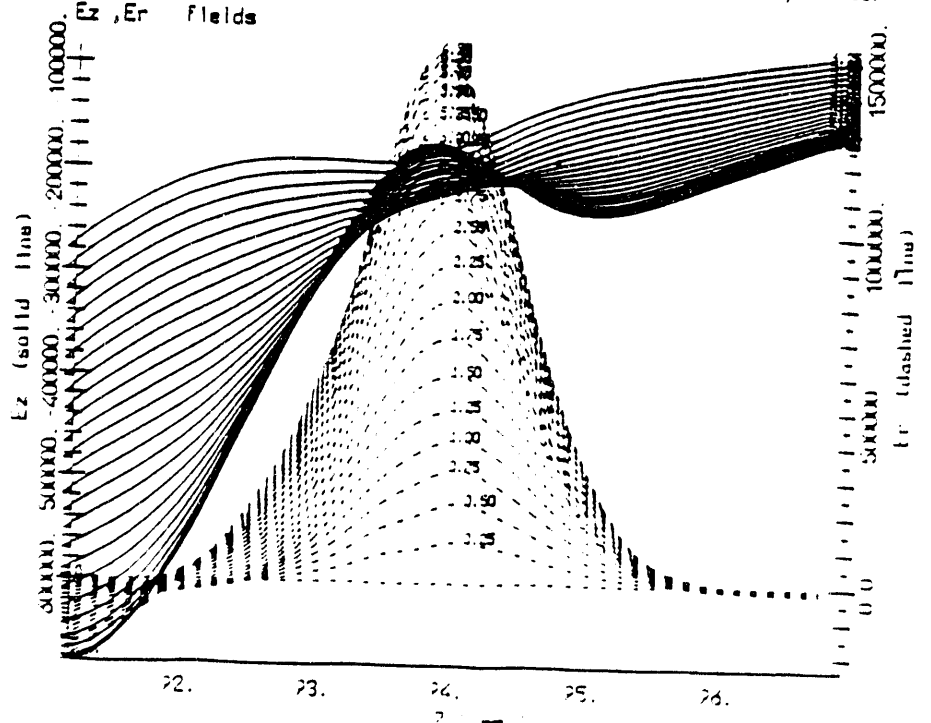

Figure X–12 Shows plot of E_z (solid line) and E_r (dashed lines) vs z. This Figure shows the electric component of the bunch self field.

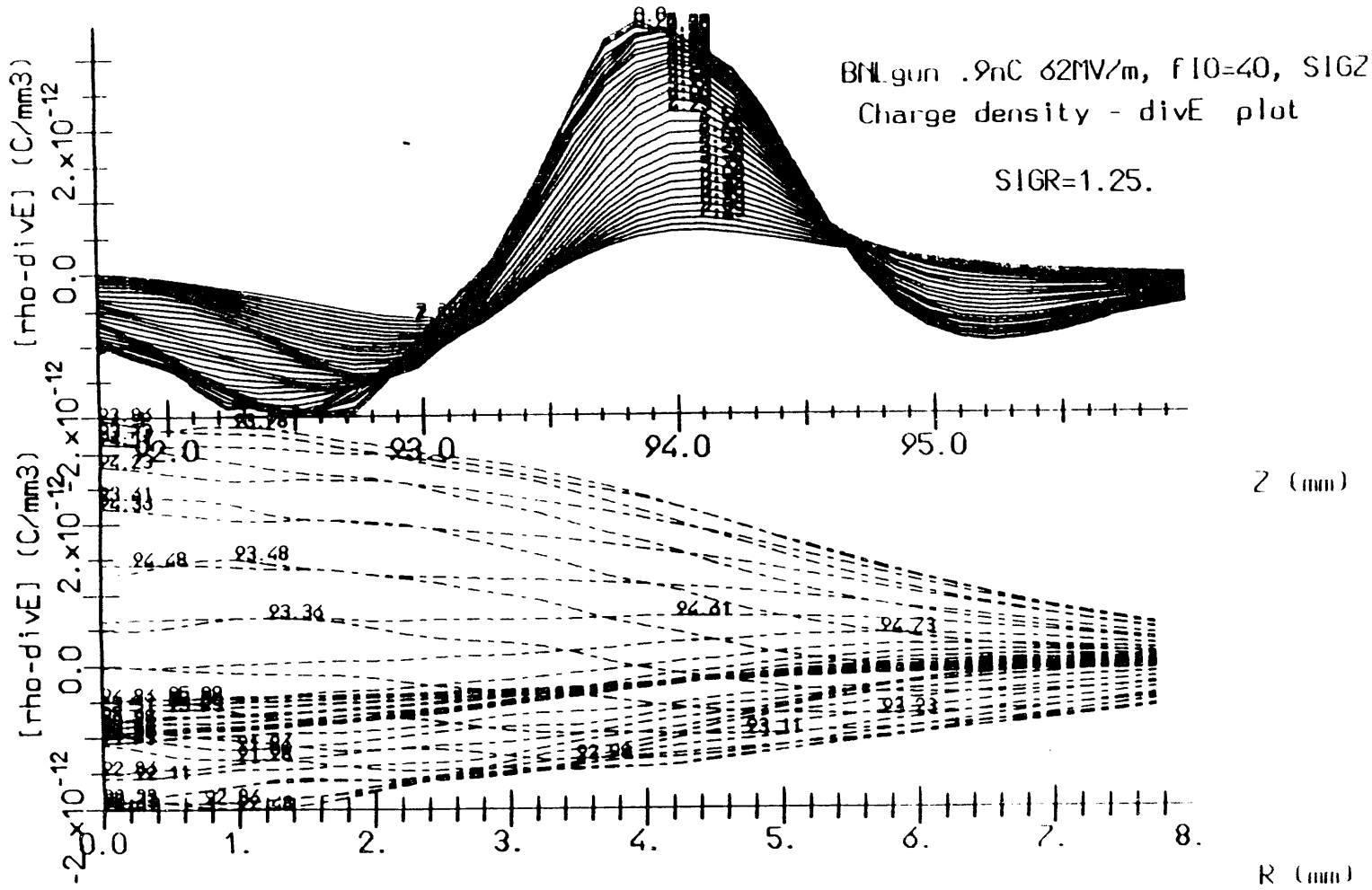

Figure X-15 Shows plot of ρ - $divE$ vs Z and R.

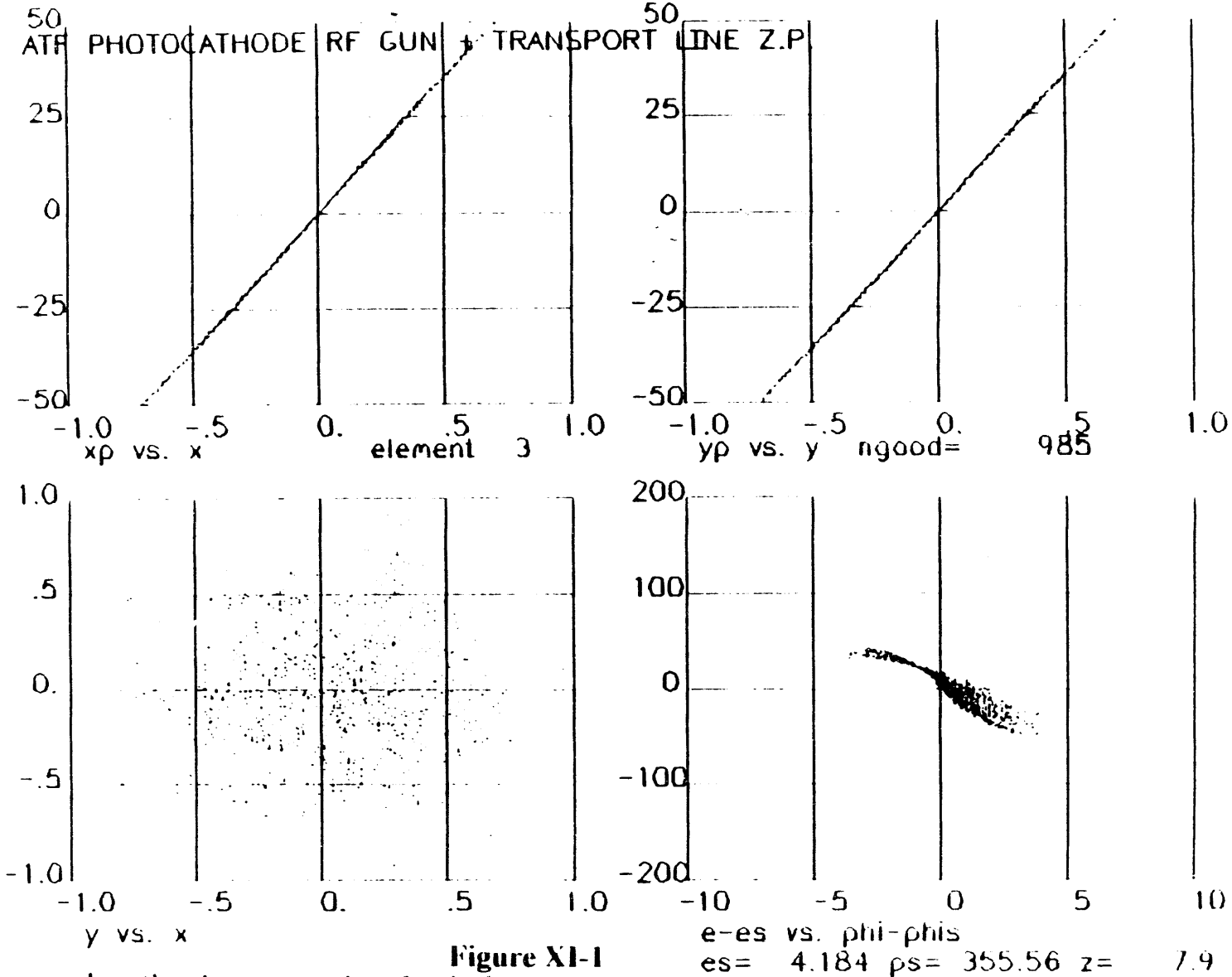

Figure XI-1

show the phase space plots for the beam at the gun exit (element 3), obtained for initial average axial electric field 66.0 MV/m, laser pulse length of $\sigma_z = 2.00°$ (2Ps), $\sigma_r = 3$mm radius, and 1 nC (design values), with the inclusion of space and image charges on the cathode. The normalized emittance (E_N^{rms}) is 0.9π cm mrad.

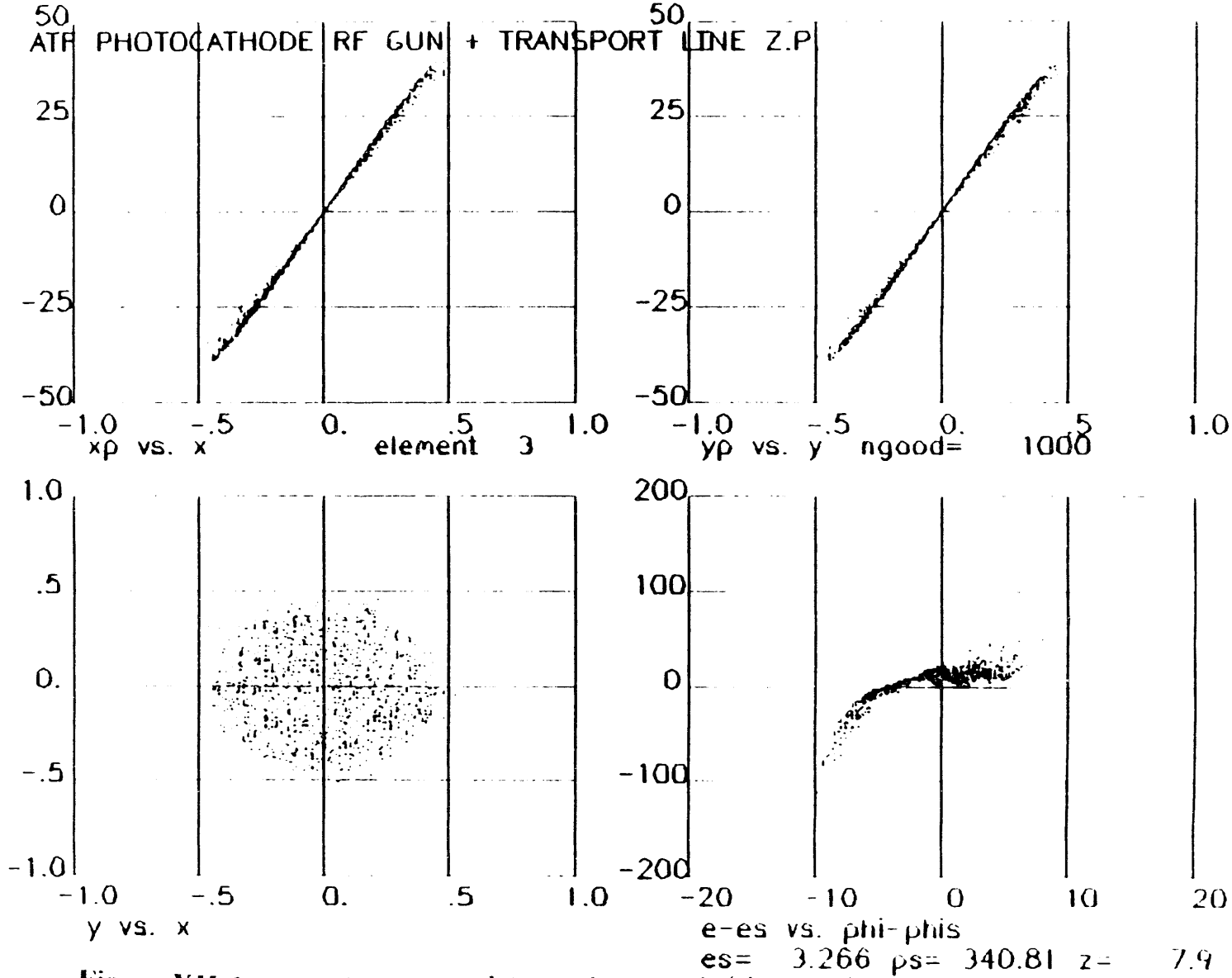

Figure XII-1 show phase space plots at the gun exit (element 3). ($\sigma_r = 1.25$ $\sigma_z = 5$Ps), charge of 2nC and the field on the cathode of 80 Mv/m (as per recent measurements)

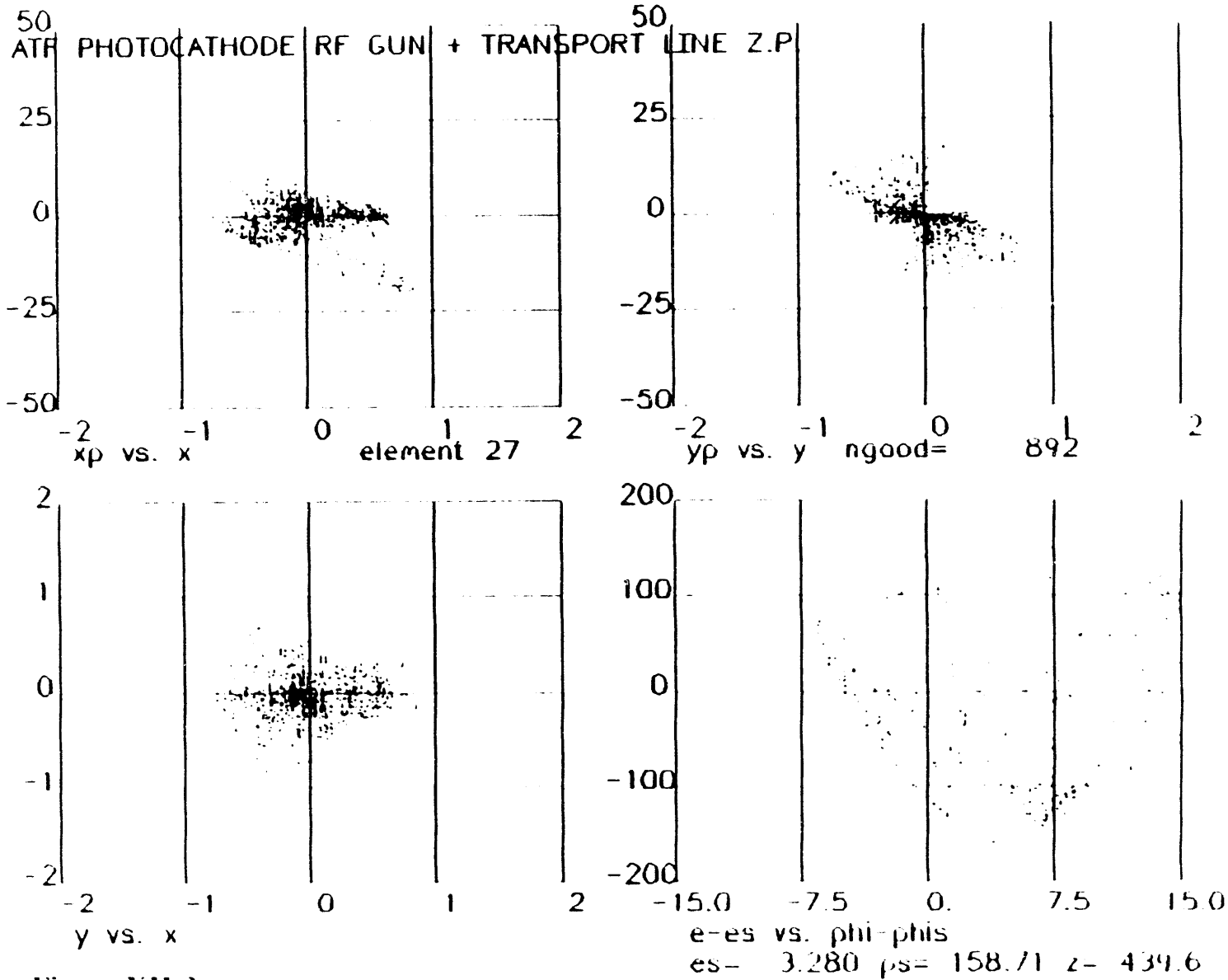

Figure XII-3 show phase space plots σ_z = 5Ps and σ_r = 1.25mm at the entrance to the LINAC the system will transfer 89 % (with 0 pole face rotation) but tunning of the 1st quads were extremely critical to get

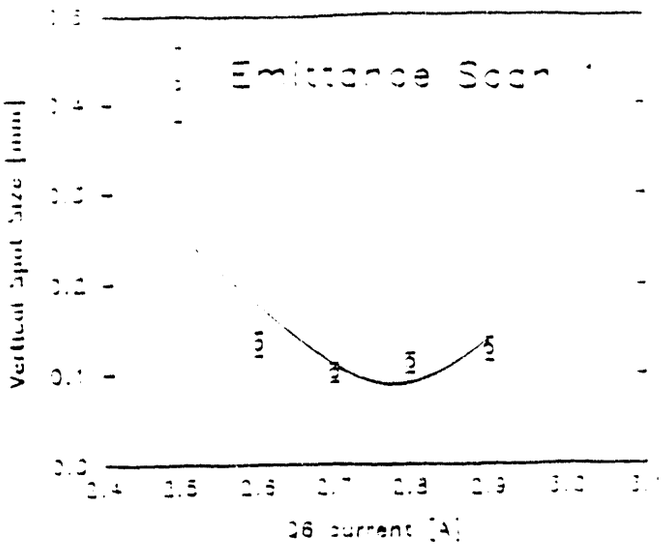

Figure XIII–1 Shows the vertical projections of the electron beam on a profile monitor as a function of quadrupole current where the measured emittance = 0.80–-0.09 mm-mrad.

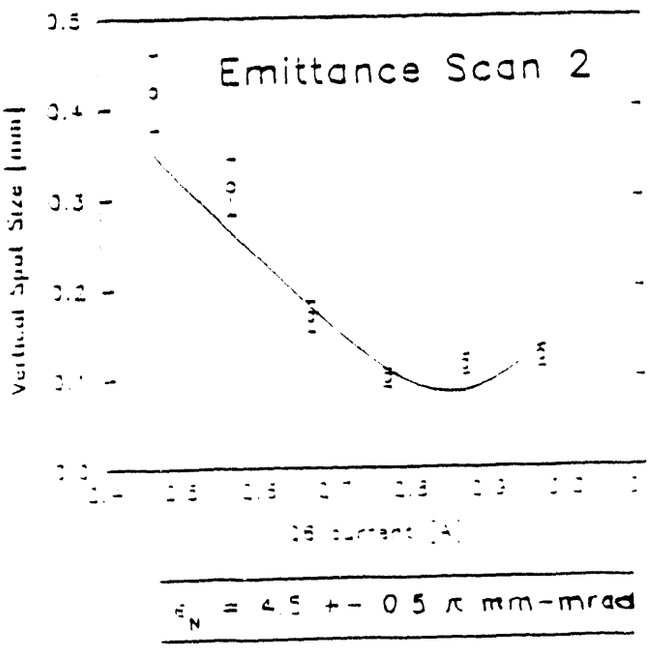

Figure XIII–2 Shows the vertical projections of the electron beam on a profile monitor as a function of quadrupole current where the measured emittance = 0.77+-0.08 mm-mrad (this figure shows a different emittance scan than those given in Fig. XIII-1).

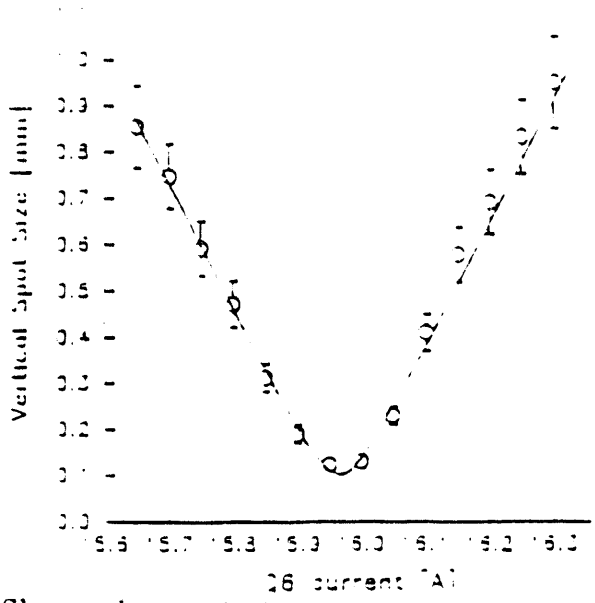

Figure XIII–5 Shows the vertical projections of the electron beam as a function of quadrupole current (this figure shows a different emittance scan than those given in Figs. XIII-1, 2 and 4).

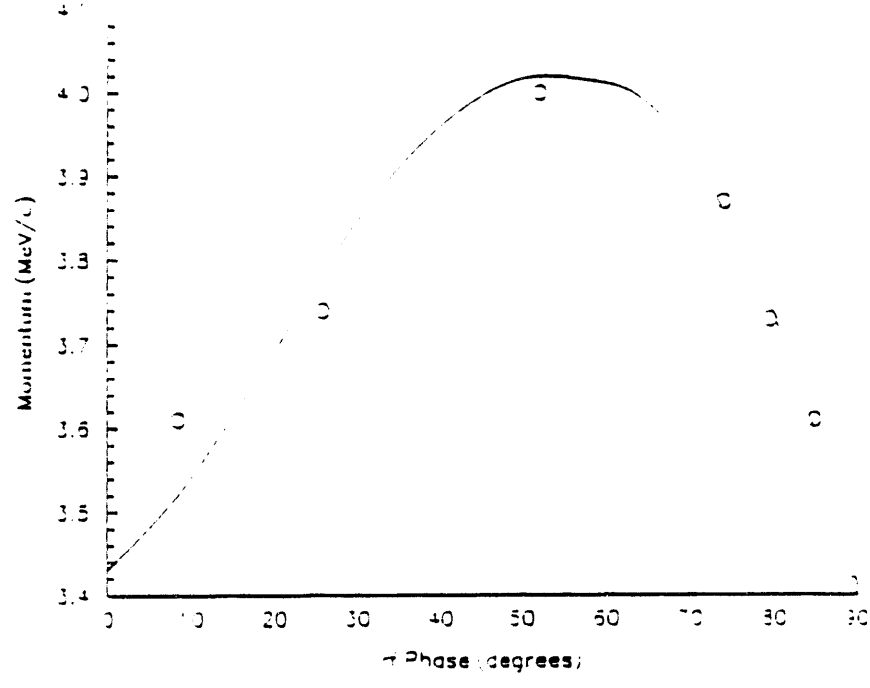

Figure XIII–6 Shows the photoelectron–beam momentum as a function of the rf phase. The data points are the momentum measured in the beamline at ATF.

END

DATE
FILMED
8/12/93